Archives of Civil and Mechanical Engineering (2023) 23:16
https://doi.org/10.1007/s43452-022-00545-y

ORIGINAL ARTICLE

Construction and dynamic identification of aeroelastic test models for flexible roofs

Fabio Rizzo[1] · Ayan Sadhu[2] · Ali Abasi[2] · Aleksander Pistol[3] · Łukasz Flaga[3] · Ilaria Venanzi[4] · Filippo Ubertini[4]

Received: 8 July 2022 / Revised: 13 September 2022 / Accepted: 1 October 2022 / Published online: 27 October 2022

Abstract
The aeroelastic wind tunnel testing of flexible roofs made of hyperbolic paraboloid cable nets is a challenging task for designers and researchers, with very limited documented experiences in the literature. The reduced-scale model construction and its dynamic identification are the main issues to address when approaching this problem, mainly because of (i) the very small mass of the roof, (ii) the strict aeroelastic criteria to satisfy and (iii) a large number of very closely spaced significant natural frequencies. To suggest an approach to follow to investigate the wind—structure interaction for this structural typology, this paper discusses the aeroelastic scaling, the aeroelastic model construction, the dynamic modal identification and the FEM predictive numerical modelling of hyperbolic paraboloid roofs (HPRs) with square, rectangular and circular plan shapes and two different curvatures. Modal identification is especially challenging due to the presence of several closely spaced modes and it is here tackled by different methods such as Welch's method, random decrement technique (RDT), Empirical mode decomposition with a time-varying filter (TVF-EMD) and frequency domain decomposition method (FDD). The satisfying accuracy of the aeroelastic scaling has been verified by comparing the wind-induced vertical displacements of the prototypes against those of the experimental models. Furthermore, an extensive qualitative investigation of the natural mode shapes has been carried out revealing that test models reproduce most of the prototype modes.

Keywords Tensile structures · Aeroelastic models · Flexible roofs · Reduced-scale model · Wind tunnel tests · Modal identification

1 Introduction

One of the main current challenges in building architecture is designing large open spaces which are suited to several activities [1, 2]. Commonly, large open spaces are used for sports arenas, concert halls and meeting rooms. The main problem for these kinds of structures is to cover a large span using the lightest structure possible. Most of the large span roofs are constructed using steel truss structures or timber structures while membrane structures or tensile structures are less common, due to the lack of technical information provided by codes and standards [3]. Consequently, a few industries work in the field of tensile structures often impeding the wide use of such structural systems by designers and practitioners. Nevertheless, considering their high structural performance, their reduced maintenance costs and their architectural attractiveness, tensile structures are closely competitive with steel or wooden structures. The lightness represents their main strength: as a matter of fact, they are often about five times lighter than an equivalent roof structure made of steel or timber [3].

There are several types of tensile structures that can be used to cover large areas, and the most common ones are grouped into two families: inflatable membrane structures and cable nets. The former is often adopted for temporary uses and typically chosen for its low cost, even if users' comfort may be a limiting factor. The latter are less widespread because it is wrongly assumed that maintenance is more

✉ Fabio Rizzo
fabio.rizzo@universityresearch.it

[1] Chair of Metal Structure L-3, Department of Civil Engineering, Cracow University of Technology, Kraków, Poland

[2] Department of Civil and Environmental Engineering, Western University, London, ON, Canada

[3] Wind Engineering Laboratory, Cracow University of Technology, Kraków, Poland

[4] Department of Civil and Environmental Engineering, University of Perugia, Via G Duranti 93, Perugia, Italy

expensive than in the case of steel or wooden structures. On the contrary, the progress that has been made in the field of cable structures has improved their reliability and longevity. The most common shape of cable net tensile structures is the hyperbolic paraboloid (HPR). The HPR cable net is made of two orders of parabolic cables, upward (load-bearing cables) and downward (stabilising cables) linked to restrain their relative vertical displacements and to permit the relative horizontal axial displacements.

Because of their lightness, HPRs are very sensitive to wind loads and, in particular, they tend to vibrate upwards and downwards under wind loading. In particular, cable instability may arise under a strong upward action, because the cable tension in the upward cables decreases until the cable becomes unstable. In the past, these kinds of roofs were constructed by covering the cable net with a reinforced concrete shell to reduce the risk of instability due to the wind flow (see Fig. 1). However, this solution strongly complicates their construction and limits their durability.

The importance of the correct modelling of the wind response of flexible roofs has been recently brought to the spotlight [1–4]. In addition, important information on wind loads for some common geometries of hyperbolic paraboloid roofs was presented [4, 5] and introduced in the Italian design standard [6].

The scientific studies in the field of HPR can be grouped into four families: (1) studies discussing the structural behaviour of the HPR cable net [1, 2, 4, 5]; (2) studies presenting the aerodynamics of HPR shape by [7] that gives parametric pressure coefficients maps for square and rectangular plan HPR with cables parallel to the roof sides and by [8] that discusses the statistics of pressure series on a square plan HPR and [9–11] that discusses the state of the art on HPR with cables at 45° with roof sides; (3) studies illustrating other multi-physics aspects, for example, the acoustic performances of HPR cable nets, as discussed by [12]; and finally, (4) studies investigating the wind-structure interaction in HPR roofs. Some examples are [13, 14] discuss the aerodynamic damping and [15] discusses the structural dynamics in terms of natural modes of HPRs made of membrane only, [16] discusses the added mass and aerodynamic damping on a square HPR made of cables and membrane, [17] investigates the behaviour of large cable roofs in the turbulent wind in the wind tunnel using both rigid and aeroelastic models and finally, [18] that investigates the aeroelastic behaviour of an open-type one-way tensioned membrane through wind tunnel tests. The Dynamics of shells with a hyperbolic paraboloid shape are also studied in different fields of engineering, for example in the geotechnical engineering field [19, 20].

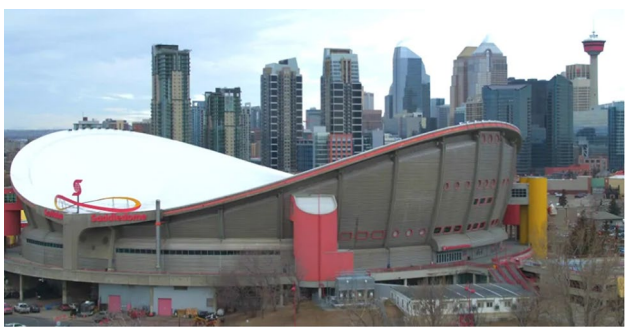

Fig. 1 Scotiabank Saddledome, 1983, Calgary, Alberta, Canada

Among the reasons why such aeroelastic studies are missing, the difficult HPR aeroelastic model construction is certainly worth mentioning. In particular, several issues complicate such a construction: (I) very small roof mass; (II) quite small structural damping; (III) geometric stiffness which is only provided by the cables; (IV) large number of natural frequencies which fall in a very narrow frequency range; (V) the need for accurate aeroelastic scaling.

This paper aims to contribute to partly filling the highlighted literature gap, focusing on aeroelastic wind tunnel modelling of HPR roofs, exclusively made of cables and membrane, with different geometries and the investigation of their dynamic response under wind loading. In particular, the paper discusses the aeroelastic scaling of the prototype, the aeroelastic reduced-scale model construction through an innovative system to apply the pre-tension to the roof and the dynamic identification of the models. Finite Element Method (FEM) numerical models are also built to support calibration and investigate the wind response of the analysed structures. The investigation is carried out concerning models with three different plan shapes (i.e. square, rectangular and circular) and two different curvatures (i.e. flatter and more sagged).

2 Prototype structural assessment

The prototype geometric sample discussed in this research was selected based on a statistical investigation carried out in reference [21] that suggested a geometrical range of the roof curvatures and plan shapes which are commonly used for tensile structures with cable nets. It was suggested that the sum $f_1 + f_2$ ranges from 1/10 to 1/8 of the $\max\{L_1;L_2\}$, where f_1 and f_2 are the upward (i.e. cables along L_1) and downward (i.e. cables along L_2) cable sags, L_1 and L_2 are the upward and downward cable spans, H_1 is the basement height and H_2 is the maximum building height. The geometrical parameters are illustrated in Fig. 2. Directions 0°, 45° and 90° are the directions of inflow during the wind tunnel experiments. Rizzo et al. [21] suggested investigating

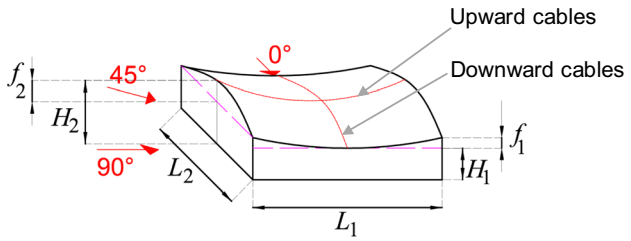

Fig. 2 Geometrical parameters

square, rectangular and circular plan shapes to cover the largest possible number of buildings.

2.1 Geometric shapes

The investigated geometric shapes are summarised in Table 1 and shown in Fig. 3. Models are named Dynamic Model (DM), square (S), rectangular (R) or circular (C), 1 (flattest roof curvature) and 2 (more sagged roof). The model DMS03 indicates a dynamic wind tunnel model with the same geometry as S02, but with the roof, the mass increased three times to investigate the aeroelastic behaviour dependence on the roof mass. In total, seven different configurations were investigated during this research: two different curvatures for each one of the three different plan shapes (i.e. square, rectangular and circular).

The maximum building height (H_2) ranges from 21.33 to 26.66 m, the maximum plan size ranges from 40 to 80 m, the upward cable sag ranges from 2.67 to 4.44 m, and the downward cable sag ranges from 5.33 to 8.89 m (Table 1). The base height is equal to 13.33 m for all geometries. In this research, the axial distance between the upward and downward cables was equal to 2 m.

2.2 Structural setup

In the cable net roof, only tensile forces act in the two orders of cables, the upward and the downward ones, which are in balance under vertical loads. The initial prestressing must ensure the roof stability under environmental loads and is calibrated to achieve the target geometrical configuration under the maximum gravitational and lifting loads.

Table 1 Geometrical parameters at prototype scale (all dimensions in [m])

Model	f_1	f_2	L_1	L_1	H_1	H_2
DMS01	2.67	5.33	80.00	80.00	13.33	21.33
DMS02	4.44	8.89	80.00	80.00	13.33	26.66
DMS03	4.44	8.89	80.00	80.00	13.33	26.66
DMR01	2.67	5.33	80.00	40.00	13.33	21.33
DMR02	4.44	8.89	80.00	40.00	13.33	26.66
DMC01	2.67	5.33	80.00	80.00	13.33	21.33
DMC02	4.44	8.89	80.00	80.00	13.33	26.66

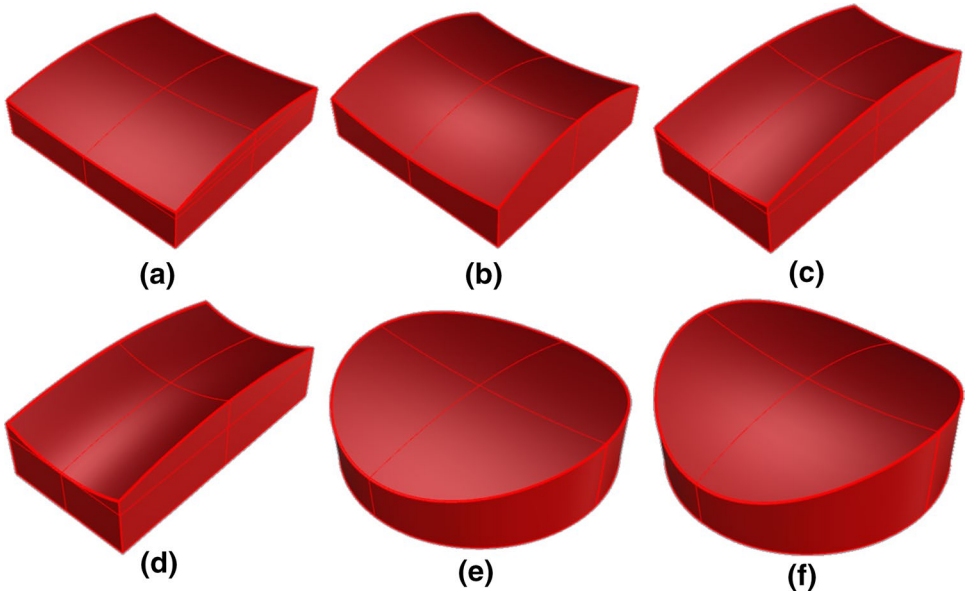

Fig. 3 Investigated samples: **a** DMS01, **b** DMS02 and DMS03, **c** DMR01, **d** DMR02, **e** DMC01 and (f) DMC02

The upward (sagging) cables are load-bearing, and the downward (hogging) cables are stabilising. Under gravitational loads, like dead loads, permanent loads or snow action, the cable net nodes tend to move upward, and this causes the stress increase in the upward cables and a consequent stress decrease in the downward cables. Under lifting wind loads (suction) the opposite occurs. Under the dynamic oscillation caused by wind fluctuation, the upward cables can lose their prestress, which may lead to a local instability of the roof that should be carefully avoided.

The main cable net's mechanical parameters are the cables' cross-sectional areas, the Young modulus of the cables, the cables' initial prestress and the Harmonic steel yield strength. In this research, to make a comparison between different geometries, cables cross sections are the same for all geometries and for both upward and downward cables. The cable's cross-sectional area was set to be equal to $1.3 \bullet 10^{-3}$ m^2. The Young modulus was set equal to $1.64 \bullet 10^5$ MPa [3, 16]. The cable strength was varied to ensure a good balance between the desired geometrical roof shape after construction (i.e. loaded with the dead and the permanent load) and an acceptable roof deformation (i.e. in the range between − 2% and 2% of the maximum cable length) under snow and wind action. The snow load was adopted as equal to 2.5 kN/m^2 and the wind action was estimated assuming the 10-min average wind speed at 10 m height equal to 30 m/s [6, 22] and using the pressure coefficients given in reference [21]. The dead and permanent load of the cable net and membrane was set equal to 0.1 kN/m^2. The initial upward cables strain was set as double the downward cables strain, between $1.5 \bullet 10^{-4}$ (DMS02, DMR02, DMC02) and $2 \bullet 10^{-4}$ (DMS01, DMR01, DMC01). The reason why the cable strain is different between upward and downward cables is that their sag is different. In particular, the sag of the downward cable (f_2) is double the upward cable sag (f_1).

2.3 Structural response

The roofs' natural frequencies were estimated through Finite Element Method (FEM) modal analyses, where the roof borders were restrained using fixed supports. Modal analyses were carried out in TENSO [4], a non-commercial software that includes modules for simulating cable and beam FEM models and for the study of wind-structure interaction phenomena with the generation of wind velocity time histories and simulation of various aeroelastic loads. The main cables were discretised as straight cable segments. The global stiffness matrix was updated at each load step by assembling the stiffness sub-matrices of the elements and accounting for the strain found at the previous time step. Through this approach, the software takes into account the geometric nonlinearity of the structure. Before the modal analysis and application of the wind loads, the TENSO software solved the structure under dead, gravity and construction load (prestressing) through nonlinear static analysis. TENSO solver employs a step-by-step incremental method and a "subsequent interaction" method with a variable stiffness matrix, which is a finite-difference approximation of modified Newton–Raphson's method for systems of nonlinear algebraic equations. According to the hypothesis of elastic behaviour of the structure under small displacements, modal analyses were carried out with the numerical FEM model considering the linearized tangent stiffness matrix under dead loads.

Figure 4 is a graphical representation of the six FEM models adopted to estimate the natural frequencies and the mode shapes. Table 2 lists the first nineteen natural frequencies calculated through modal analyses. It can be seen that the natural frequencies of the first 19 modes are in a very close range.

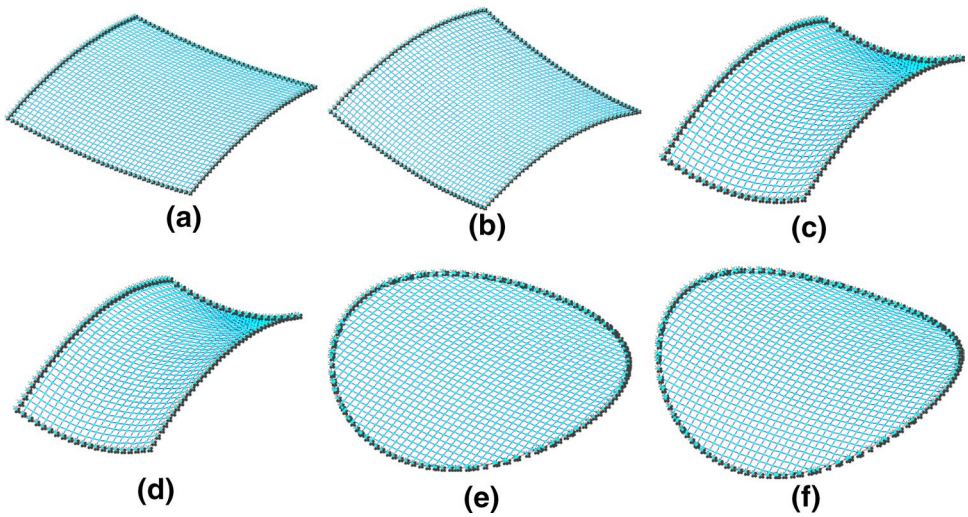

Fig. 4 Roof FEM models: **a** DMS01, **b** DMS02 and DMS03, **c** DMR01, **d** DMR02, **e** DMC01 and **f** DMC02

Table 2 Structural natural frequencies

Mode	DMS01		DMS02 and DMS03		DMR01		DMR02		DMC01		DMC02	
	n (Hz)	Mp (%)	*n* (Hz)	Mp (%)	*n* (Hz)	Mp (%)	*n* (Hz)	Mp (%)	*n* (Hz)	Mp (%)	*n* (Hz)	Mp (%)
#1	0.23	< 1	0.18	< 1	0.12	0.64	0.09	1.47	0.23	< 1	0.18	< 1
#2	0.24	< 1	0.19	< 1	0.21	< 1	0.16	< 1	0.24	< 1	0.18	< 1
#3	0.25	< 1	0.20	< 1	0.21	< 1	0.16	0.01	0.25	< 1	0.19	< 1
#4	0.26	< 1	0.21	< 1	0.21	< 1	0.16	0.77	0.26	< 1	0.20	< 1
#5	0.28	< 1	0.23	< 1	0.21	< 1	0.16	0.00	0.27	< 1	0.21	< 1
#6	0.30	0.06	0.24	< 1	0.21	< 1	0.16	0.00	0.28	< 1	0.21	< 1
#7	0.30	0.07	0.26	0.31	0.21	**83.69**	0.17	0.00	0.29	< 1	0.22	< 1
#8	0.31	**15.83**	0.26	2.25	0.21	0.57	0.18	**88.36**	0.30	< 1	0.23	< 1
#9	0.31	0.49	0.26	**34.47**	0.22	2.11	0.18	0.97	0.31	0.01	0.24	< 1
#10	0.32	0.49	0.27	0.54	0.22	0.60	0.18	1.47	0.31	0.04	0.24	< 1
#11	0.33	**22.01**	0.27	1.66	0.22	1.44	0.19	1.23	0.32	0.36	0.25	0.01
#12	0.33	0.56	0.28	**22.28**	0.23	1.84	0.19	1.16	0.32	1.82	0.25	0.04
#13	0.34	0.08	0.29	0.11	0.24	1.58	0.20	0.96	0.32	**32.44**	0.26	0.30
#14	0.35	2.59	0.29	0.34	0.24	1.92	0.21	2.15	0.33	1.39	0.26	0.26
#15	0.35	0.20	0.30	**19.27**	0.24	1.79	0.21	0.58	0.34	0.31	0.26	**20.44**
#16	0.36	**26.10**	0.31	0.93	0.25	2.01	0.22	0.23	0.34	4.88	0.27	0.93
#17	0.37	0.09	0.32	0.01	0.25	0.33	0.23	0.14	0.34	**54.07**	0.27	1.06
#18	0.38	**30.45**	0.33	0.69	0.25	0.62	0.23	0.06	0.35	4.06	0.27	2.27
#19	0.39	0.99	0.33	**17.15**	0.26	0.85	0.23	0.42	0.35	0.62	0.27	**74.69**

The frequency ranges from 0.09 (DMC02) Hz to 0.16 Hz (DMS01). The first natural frequency varies from 0.09 Hz (DMR02) to 0.23 Hz (DMS01 and DMC01). It was observed that the models with more sagged roofs exhibit smaller natural frequencies than the models with flatter roofs. This is explainable because models with flatter roofs were designed with stiffer cable nets employing higher levels of prestress.

The natural modes with the biggest participating mass ratios correspond to the modes involving the largest area of the roof [4] and were considered in this research as significant structural modes.

The first 19 natural frequencies, their participating modal factors and participating mass percentages are listed in Table 2. The participating modal factors Γ_j were estimated according to Eqs. (1) and (2), where Φ_j are the eigenvectors, M_j is the diagonal mass matrix, the quantity $\widehat{M_j} = \Phi_j{}^T \bullet M_J \bullet \Phi_j$ is the modal mass, and *R* is a vector of unit modulus and it indicates the direction of the force only [16].

$$\Gamma_j = \frac{\Phi_j{}^T \bullet M_j \bullet R}{\Phi_j{}^T \bullet M_j \bullet \Phi_j} \tag{1}$$

$$M_{p_j} = 100 \bullet \frac{\Gamma_j{}^2 \bullet \widehat{M_j}}{\sum_{j=1}^{n} \widehat{M_j}} \tag{2}$$

It was observed that the participating mass ratio varies significantly between models with different plane shapes. Models with a square plan shape have four modes with a significant participating mass ratio ranging from about 16% to about 35%. Models with a circular plan shape have only two modes with a significant participating mass ratio ranging from about 21% to about 75%. Finally, models with rectangular plan shapes have only one mode with a significant participating mass ratio in the range between 83 and 89%. With the assumption that the mode with the biggest participating mass ratio is the global mode of the cable net because it involves the largest surface of the roof, it can be concluded that the roof with a rectangular plan shape has only one global mode in the range of investigated nineteen modes.

Figure 5 presents the mode shapes with the maximum participating mass ratios for each model. As can be observed, there is an agreement between the values listed in Table 2 and the roof modal shapes for each geometry. Figure 5 shows that for the case of a square plan roof, the mode with the largest participating mass ratio is very different between the flatter roof (DMS01) and the more sagged roof (DMS02), whereas on the contrary, the deformed shape is very similar for the rectangular and circular shape roofs. This means that it is expectable that the dynamic responses of models DMS01 and DMS02 are significantly different due to the roof curvature and cable net stiffness.

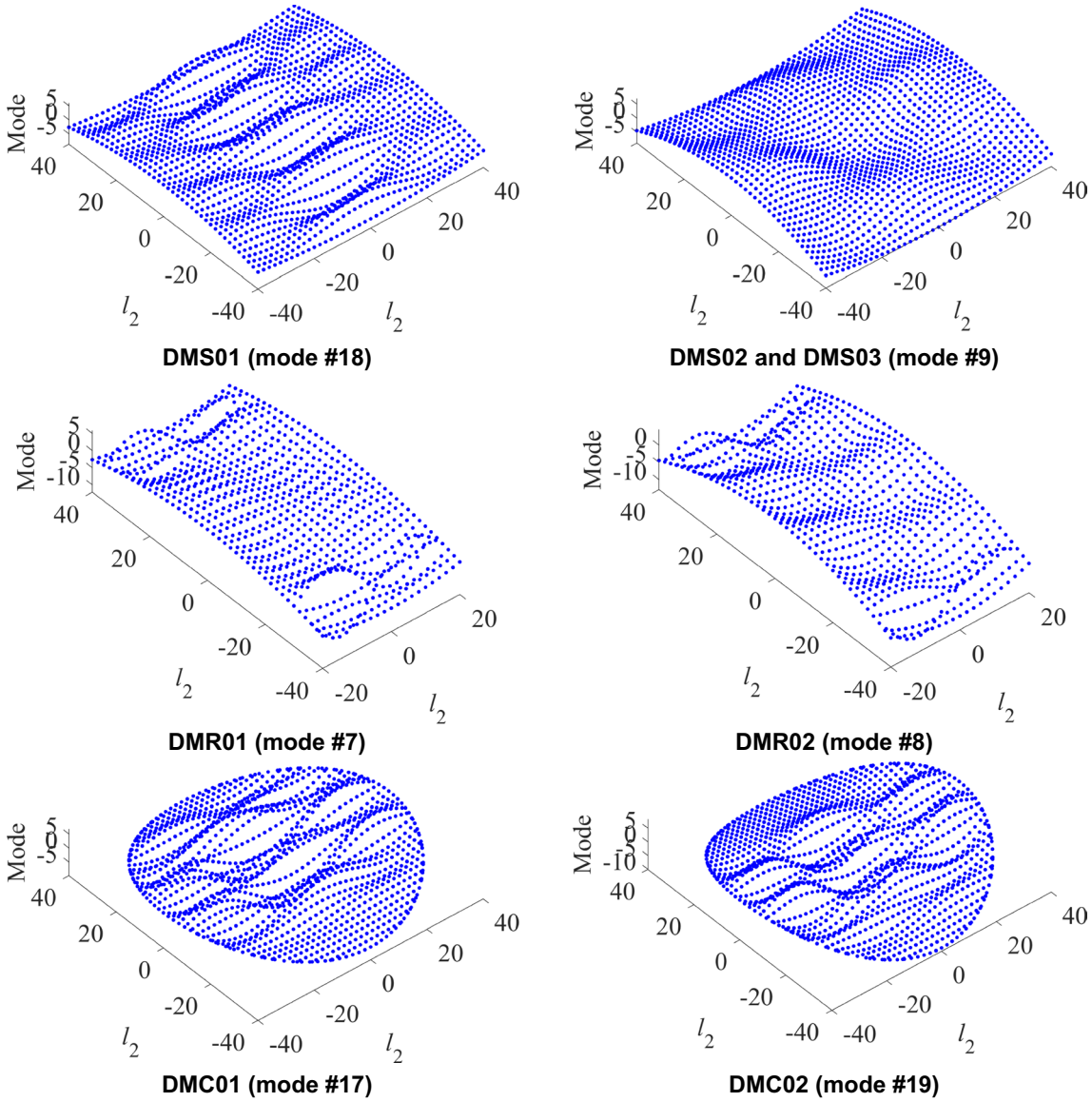

Fig. 5 Modal deformed shape with the maximum participating mass ratio

3 Aeroelastic scaling and experimental models' setup

3.1 Aeroelastic criteria

The aeroelastic models for dynamic wind tunnel tests were designed according to aeroelastic scaling requirements [23]. Aeroelastic models require similarities in geometry, inertia/mass distribution, damping and stiffness, and these must be consistent with flow scaling in the wind tunnel. The following modelling criteria were closely followed in the case of the roofs studied herein. Equation (3) defines the translational mass ratio between model and prototype (λ_m) as a function of the geometrical scale (λ_L):

$$\lambda_m = {\lambda_L}^3 \tag{3}$$

The speed scaling parameter, λ_V, is defined as given in Eq. (4); the natural frequency parameter, λ_η, is the ratio between the model and prototype first natural frequencies [23].

$$\lambda_V = \lambda_L \lambda_\eta \tag{4}$$

The geometrical scale, λ_L, was adopted as 1:200 and the desired model characteristics were designed taking into account the need to have the smallest possible roof mass and to have a sufficiently large first natural frequency to obtain a not-too-low wind velocity at roof height (Eq. 4). This goal

was achieved using specific materials and mechanical techniques [16].

According to Eq. (3), the mass scale, λ_m, was estimated to be equal to $(1/200)^3 = 1.25 \bullet 10^{-7}$. Aeroelastic scaling requires the damping ratio to be the same between the model and prototype. However, the damping of cable nets and membrane roofs is not discussed in codes and literature only gives values for some specific cases [16]. Overall, it is reasonable to assume that the structural damping of cable roof structures is greater than that of conventional steel structures or suspension bridges. This is due to the effect of the membrane, which is linked to the cables through connectors. These typically exhibit a non-linear behaviour where the increase in tension also causes an increase in structural damping [16] essentially due to friction. This aspect affects the results of the study of tensile structure dynamics.

The literature, however, does not give a maximum expected value and, in addition, an exact value can only be estimated with full-scale measurements.

As will be thoroughly discussed in the next sections, model materials and mechanical settings were designed step-by-step through an iterative process while monitoring frequencies and damping.

3.2 Experimental models description

Aeroelastic models for wind tunnel testing were constructed according to the criteria discussed in Sect. 3.1. The building walls were made of stainless steel with a thickness equal to 2 mm. The roof was made of steel prestressed ropes and a silk fabric sewed to the ropes net (but not connected to the steel structure to avoid an increase in structural damping). Each rope net node was connected to release the relative horizontal movement and to fix the relative vertical displacements. The Young modulus of the steel rope was estimated experimentally, through axial tests, yielding a value of $1.65 \bullet 10^4$ MPa. Figure 6 illustrates the mechanical system used to prestress the ropes. Upward and downward ropes were strained through a complex system of bolts that were screwed into steel couplings mounted into timber slats.

On one end, each steel rope was fixed to the bolt through a loop protected by a Teflon tube and between two nuts to avoid the rope rotation around the bolt axis. On the opposite end, the steel rope was fixed to the model lateral surface made of steel plates through a loop protected by a Teflon tube and fixed by a clamp. The rope prestressing was obtained by screwing the bolt into the steel coupling clockwise.

The exact prestress given to the steel rope was estimated geometrically. It is the necessary value to obtain the desired geometry of the net. It was achieved using wooden moulds of desired shapes. At first, upward ropes were connected with a straight profile. Subsequently, the downward ropes were connected and strained to move down the upward ropes until reaching the wooden mould. During this phase, the strain in the upward ropes increased, and it was necessary to preliminary design the necessary strength to avoid rope rupture.

Once the cable net was constructed (Fig. 7a), it was covered by silk fabric sewn to the nodes of the net (Fig. 7b). The silk material was chosen for its lightness as its surface mass was equal to about 97 g/m^2.

Even if the fabric is very light, its weight still affects the roof mass because the contribution of ropes is negligible. The steel ropes' diameter was equal to 0.3 mm for all models except for model DMS03, where it was equal to 0.5 mm, and the rope's net mass per square meter was about 1.1 g/m^2. The total roof mass per square meter was equal to about 98 g/m^2.

Figure 7 shows all the models with and without fabric and Table 3 lists the wind tunnel model dimensions (indications as per Fig. 2). It was observed that the structural damping of the model increased when the ropes were connected together to obtain a net through the cotton thread, but it was not affected by the silk fabric connection to the rope net. This outcome was expected because the silk fabric was not connected to the borders of the model and because the roof mass increases when the ropes are connected together. Since the silk fabric is not connected to the model steel borders, thin silicon joint will be necessary during wind tunnel tests to avoid the wind lifting of the silk fabric, which would cause undesired effects [16].

4 Models' dynamic identification

4.1 Free vibration signals acquisition and frequency spectra

The dynamic identification of the models to estimate natural frequencies and structural damping was carried out by using the recorded roof accelerations in ambient vibrations. This approach was found suitable because several natural frequencies were identified on the spectra, in agreement with FEM modal analysis results. Four small, very light (0.8 g) and sensitive (100 mV/m/s^2, 1–8 kHz) accelerometers model 352A24 PCB PIEZOTRONICS were used for the modal identification. The number of sensors simultaneously mounted on the roof was reduced to 4 during each measurement to avoid altering the roof mass with their weight. Signals were acquired with a sampling frequency equal to 1000 Hz (setup A, Fig. 9a) and 1600 Hz (setup B, Fig. 9b) and with a total length equal to 1800s (setup A) and 300 s (setup B). Accelerometers were fixed to the roof through four magnets placed under the roof and four magnets attached to the accelerometers by tape. Figure 8 shows the two experimental setups considered in this study.

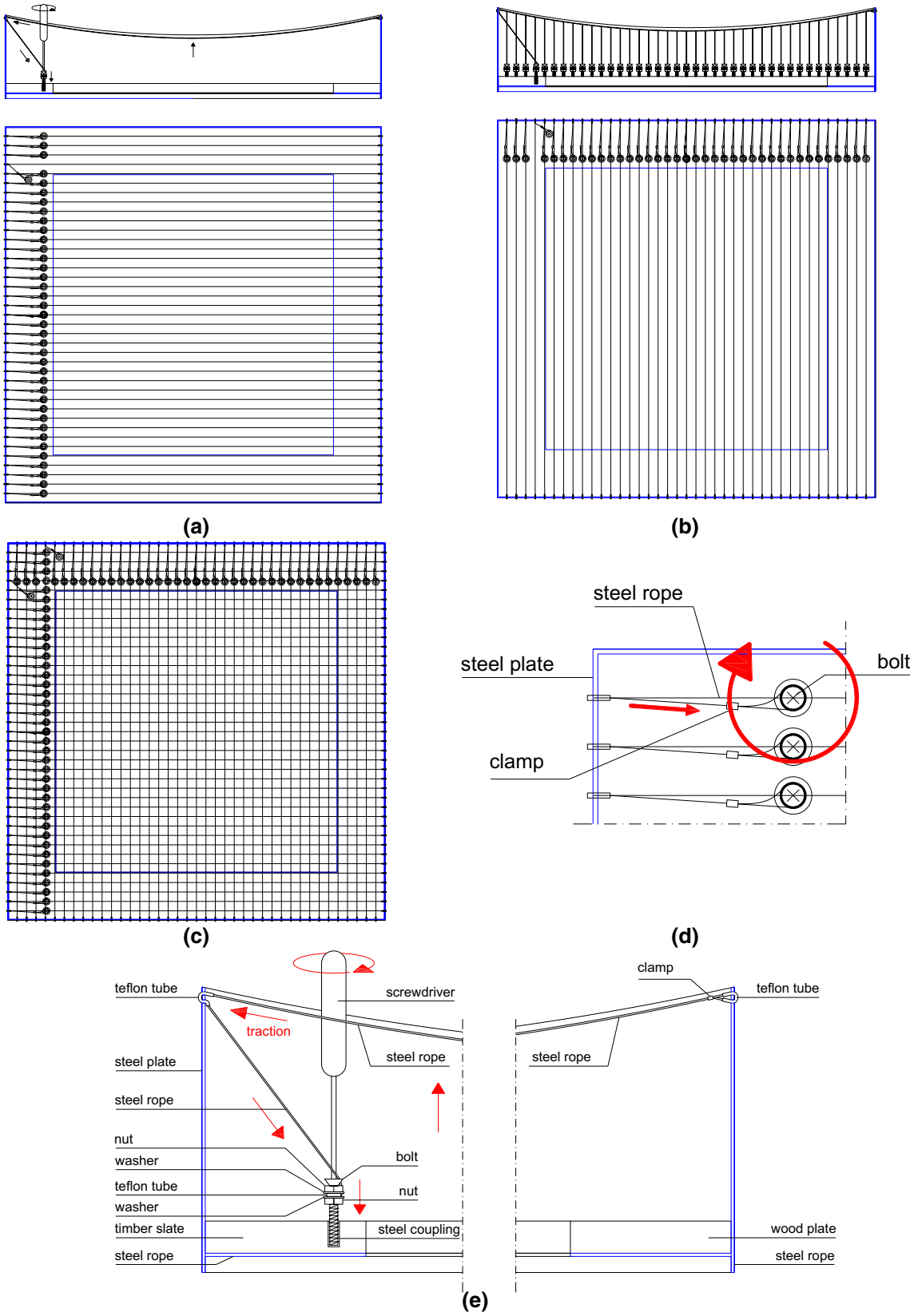

Fig. 6 Model construction setup: **a** upward ropes, **b** downward ropes, **c** entire cable net, **d** rope prestressing detail, **e** detail of the system used for prestressing the ropes

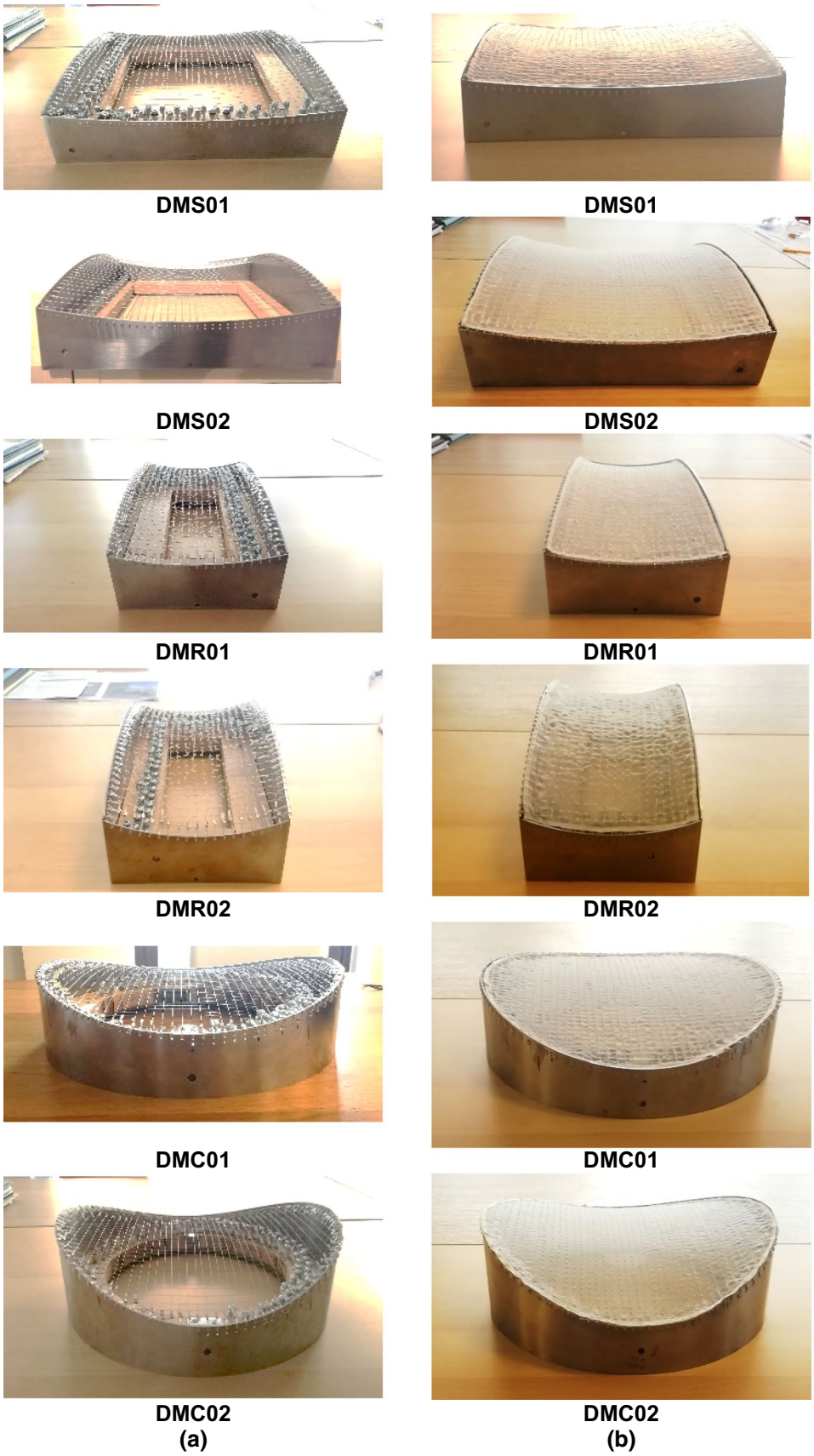

Fig. 7 Experimental models: **a** cable net, **b** cotton fabric roof

Table 3 Wind tunnel models dimensions (dimensions in [cm])

Model	f_1	f_2	L_1	L_2	H_1	H_2
DMS01	13.4	2.67	40.00	40.00	66.7	106.7
DMS02	22.2	4.44	40.00	40.00	66.7	133.3
DMS03	22.2	4.44	40.00	40.00	66.7	133.3
DMR01	13.4	2.67	40.00	20.00	66.7	106.7
DMR02	22.2	4.44	40.00	20.00	66.7	133.3
DMC01	13.4	2.67	40.00	40.00	66.7	106.7
DMC02	22.2	4.44	40.00	40.00	66.7	133.3

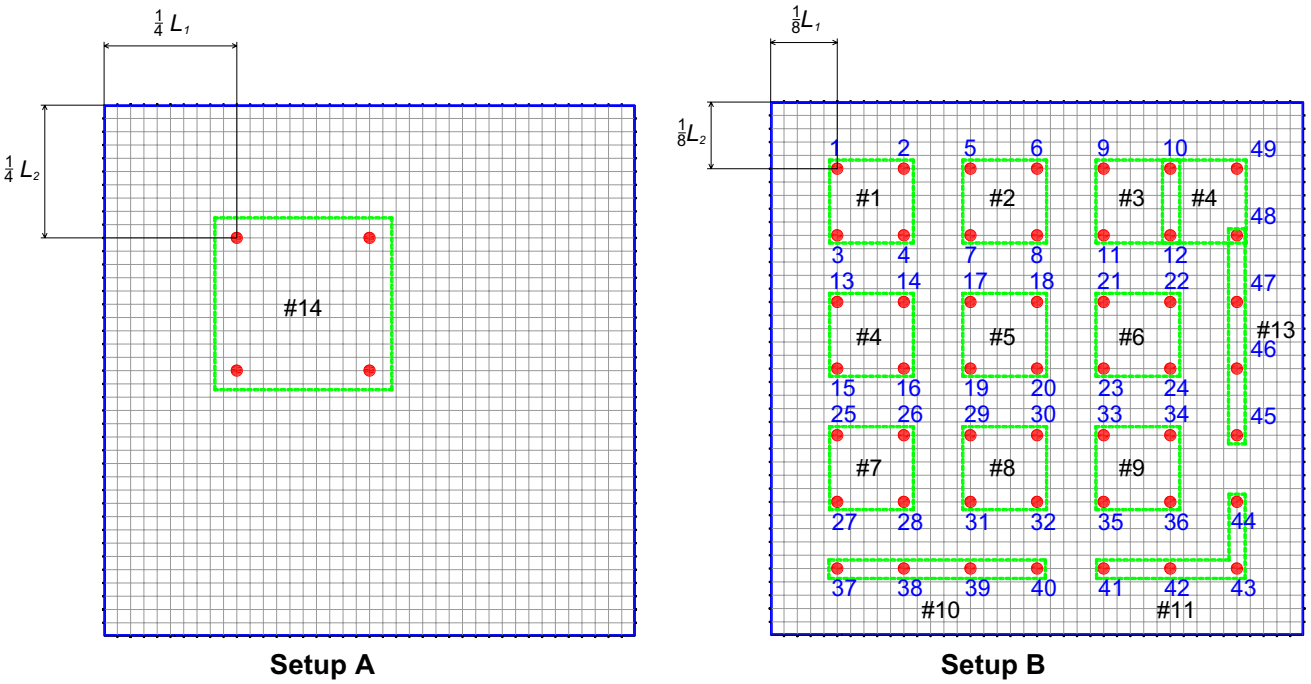

Fig. 8 Sensors setup configurations

The experimental setup A was used to acquire data at 4 positions relative to a square area $1/4L_1 \times 1/4L_2$. The experimental setup B was adopted to record signals on a 5-by-5 square grid $1/8L_1 \times 1/8L_2$ for a total of 49 different positions.

Figure 9 shows the experimental setup A for models DMS02 and DMR01. For the sake of brevity, only the results provided by setup A for all models and results provided by setup B for model DMS01 are discussed in this paper; for this case, the smallest and the largest relevant frequencies for the investigated roofs were observed.

Figures 10 and 11 show the power spectral densities (PSD) obtained by the Welch method on the acquired accelerometric signals filtered through a band-pass Butterworth filter with cut-off frequencies equal to 1 and 50 Hz. Table 4 summarises the first three resonant frequencies estimated for all models. Results confirmed that models with a flatter curvature have frequencies slightly larger compared to more curved models, as was observed through FEM numerical analyses.

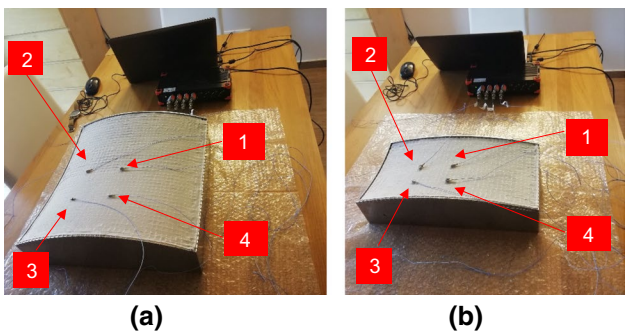

Fig. 9 Experimental setup A: DMS02 (**a**), DMR01 (**b**)

The first three frequencies were close to 11 Hz, 13 Hz and 26 Hz in most cases. Comparing the frequency spectra

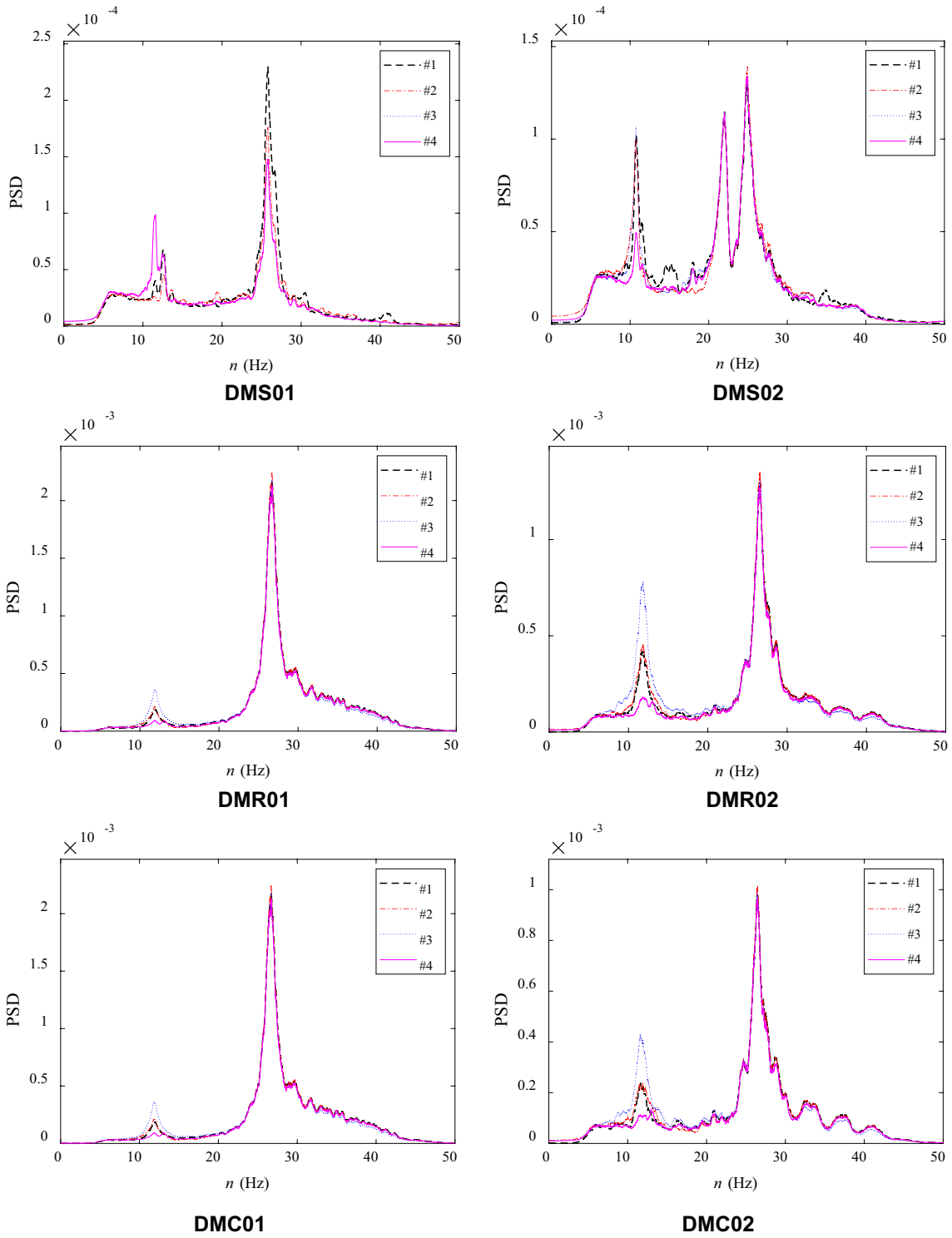

Fig. 10 Power spectral density (a^2/Hz) of recorded signals in Setup A for all the investigated geometries

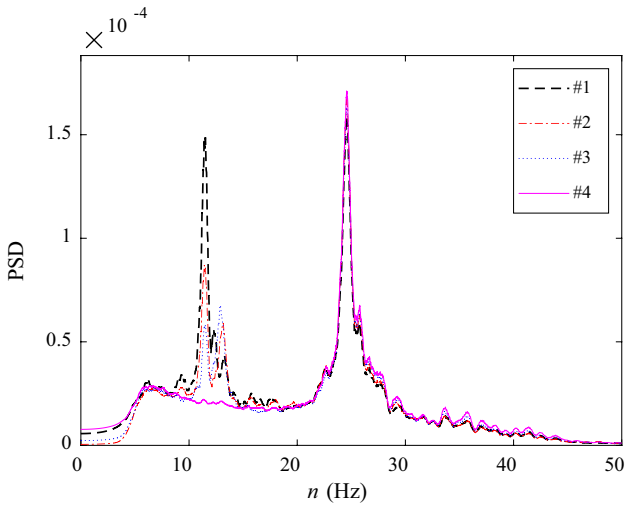

Fig. 11 Power spectral density (a^2/Hz) of model DMS03, setup A

obtained for DMS02 (Fig. 10) and DMS03 (Fig. 11), it was observed that there is an additional frequency of around 22 Hz for model DMS02 (Table 4).

Table 4 lists the frequencies estimated through the Welch method using setup A for all investigated geometries. It was observed that frequencies are quite similar for all models and that the first two frequencies are very closely spaced.

Figure 12a, b and c show examples of Power Spectral Density, whereas Fig. 12d shows the number of occurrences of frequencies estimated using setup B. The number of different frequencies estimated by experiments through setup B is larger than their number from setup A, which is in agreement with the modal analyses results discussed in Sect. 2.3.

4.2 Damping ratio estimation through random decrement technique (RDT)

Signals were processed after filtering (i.e. bandpass filter with cut-off frequencies equal to 1 and 50 Hz) to evaluate damping and frequency to estimate the damping ratio corresponding to the most relevant frequencies. The random decrement technique (RDT) is a time-domain signal processing approach utilised for evaluating the free vibration response of a dynamic system [24] by determining a characteristic signature from the ensemble average of preselected sample segments from random response signals. The RDT is based on the hypothesis of a zero-mean stationary Gaussian Process. The expectation operation of the sub-response can approximately be written as [24]:

$$E[X(t)] \approx \frac{1}{N}\sum_{i=1}^{N} x(t_i + \tau) \tag{5}$$

where N represents the subsample, $\tau = t - ti$ and $x(t)$ is the dynamic response of the structure subject to ambient excitation; constant time segments $[ti, ti + \tau]$ were extracted from the dynamic response $x(t)$ every time the signal amplitude reached a certain crossing level $x0$. Averaging N segments of the response measurements yielded a time function called the RDT signature function defined as:

$$\delta(t) \approx \frac{1}{N}\sum_{i=1}^{N} x(t_i + \tau) \tag{6}$$

To perform a parametric identification, the RDT signature can be expressed as:

$$\hat{\delta}(t) \approx \frac{1}{N}\sum_{i=1}^{m} e^{a_i t}(c_i cos(b_i t) + d_i sin(b_i t)) \tag{7}$$

where m is the considered mode order and a_i, b_i, c_i and d_i are unknown parameters to be determined. To optimise the RDT signature, an error function is defined as follows:

$$G(\kappa) = \frac{1}{M}\sum_{j=1}^{M}\left[\sum_{i=1}^{m} e^{a_i t}(c_i cos(b_i t) + d_i sin(b_i t))\right]^2 \tag{8}$$

where M is the number of the measured points and κ represents the unknown parameters vector defined as:

$$\boldsymbol{\kappa} = a_i \ldots a_m b_i \ldots b_m c_i \ldots c_m d_i \ldots d_m \tag{9}$$

Table 4 Setup A scaled model structural natural frequencies (Hz), f, via Welch method and damping ratio trough random decrement technique (RDT), ς

Mode	DMS01	DMS02	DMS03	DMR01	DMR02	DMC01	DMC02
f (Hz)							
#1	11.6	10.7	11.4	11.9	11.7	11.8	11.5
#2	12.6	12.5	12.9	13.2	13.1	12.9	12.7
#3	25.8	24.9	24.6	26.7	26.5	26.7	26.4
ς (%)							
#1	2.4	3.2	3.1	2.5	3.2	2.3	2.1
#2	1.7	2.3	3.2	1.4	1.8	2.6	2.3
#3	2.3	3.8	3.7	1.0	1.8	2.1	3.2

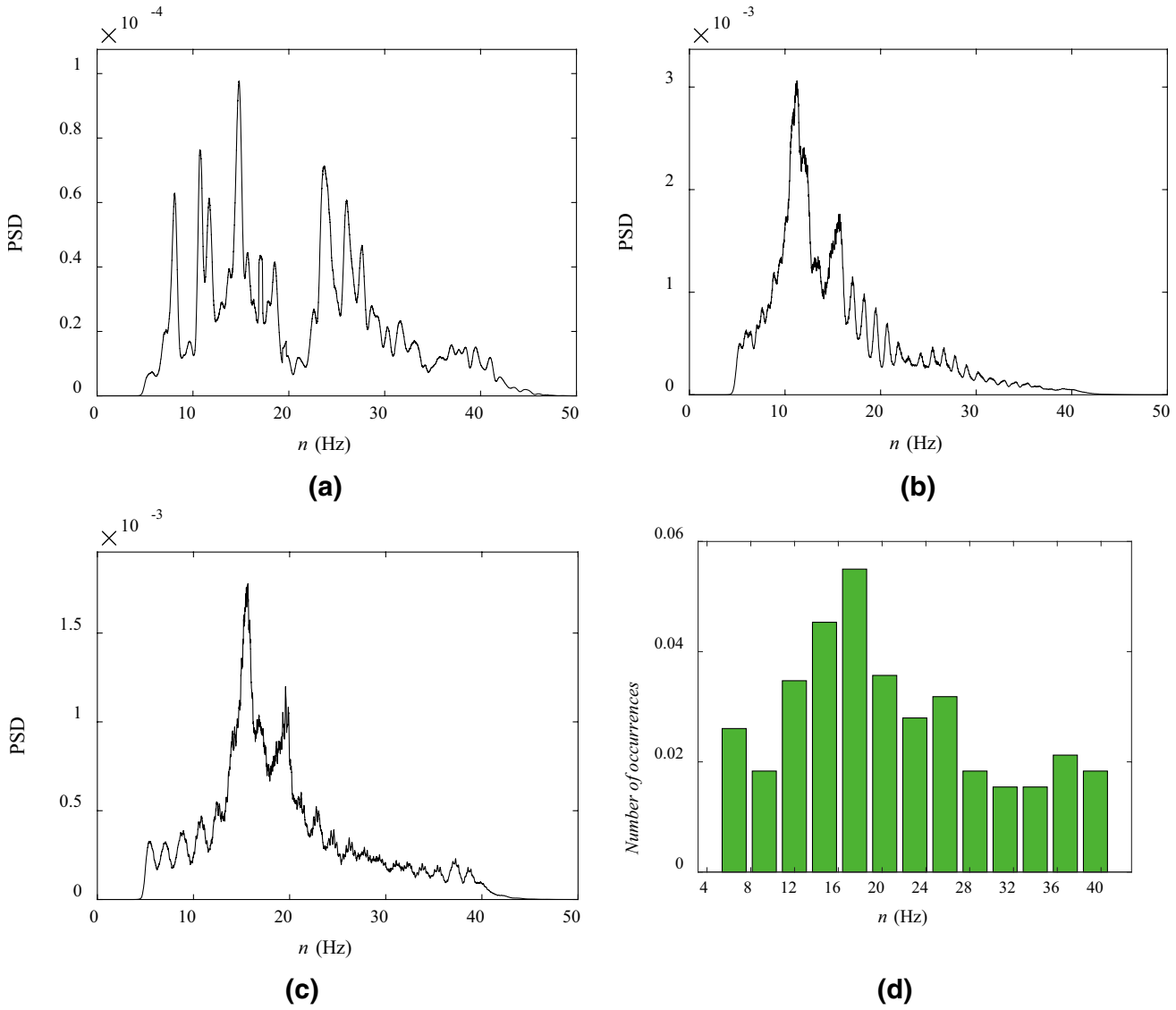

Fig. 12 **a**–**c** Power spectral density (a^2/Hz) of some signals (#14, #18 and #46) acquired using the Setup B for geometry DMS01, **d** number of occurrences of frequencies estimated using setup B

A nonlinear fitting approach was applied to minimise G (κ function). Once vector κ was determined, modal parameters of the examined model were found through the following relationship:

$$a_i = -\omega_i \sqrt{1 - {\xi_i}^2} \tag{10}$$

As:

$$\omega_i = \left(\sqrt{{a_i}^2 + {b_i}^2} \right) \xi_i \tag{11}$$

where ωi and ξi are the undamped modal frequency and damping ratio of the considered i-th mode. It was assumed that the approximation from MDOF to SDOF was acceptable because the investigation focused on some specific frequencies recognised as significant from modal analyses [16]. Figure 13 shows an example of the application of the RDT technique and Table 4 shows the damping ratios for each geometry and frequencies estimated via the Welch method.

4.3 Dynamic identification of models via TVF-EMD

Empirical mode decomposition (EMD) decomposes a multi-component signal into a set of oscillatory waveforms known as IMFs [25]. The typical mode-mixing problem of EMD can be resolved using a time-varying filter (TVF) [26, 27], where the cut-off frequency of a TVF is designed to be time-varying, which makes it suitable for nonstationary

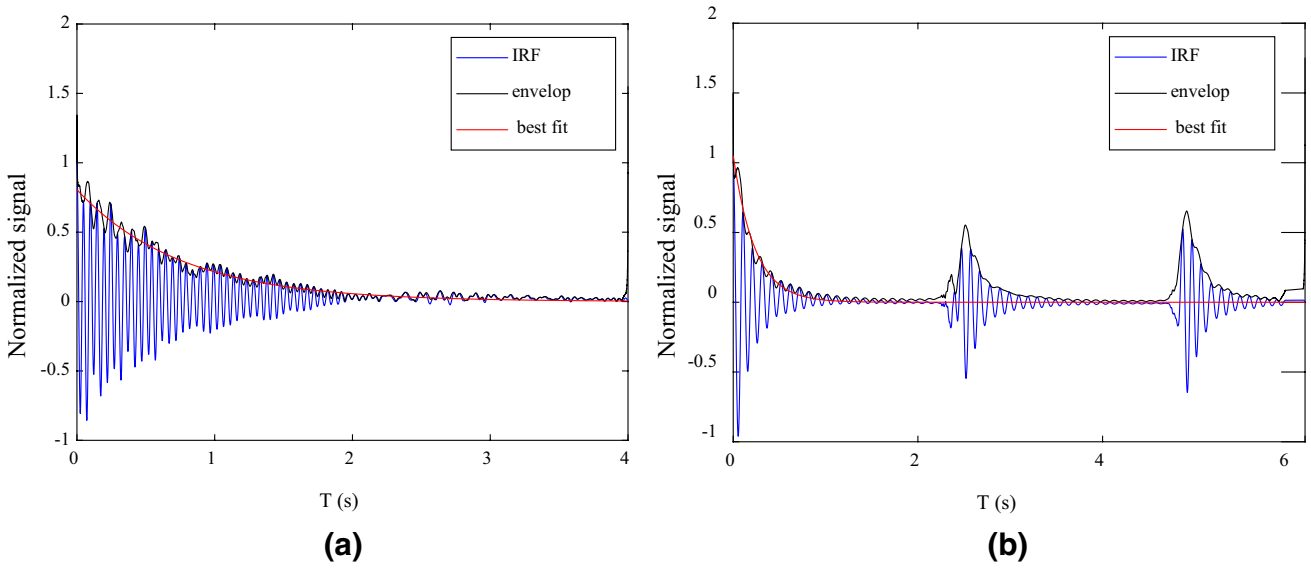

Fig. 13 Random decrement technique, envelop of the curve with the Hilbert transform, DMS02 (**a**) and DMR02 (**b**)

time-series data. In TVF-EMD, each signal can be estimated in B-spline space by a method shown in Eq. 12 [26–28]:

$$b_v^p(t) = \sum_{j=-\infty}^{+\infty} q(j)\beta^p\left(\frac{t}{v} - j\right) \tag{12}$$

where $q(j)$ are the B-spline coefficients, and they are magnified by a factor of v, which is the step size of the knot sequence. The signal is determined by p, v, and $q(j)$. The B-spline coefficients $q(j)$ are obtained by using the B-spline approximation that minimises the estimation error. For an original signal $y(t)$, $q(j)$ is determined by minimising the estimation error δ_v^2:

$$\delta_v^2 = \sum_{j=-\infty}^{+\infty} \left(y(t) - \{q\}_{\uparrow v} * w_v^p(t)\right)^2 \tag{13}$$

where $\{q\}_{\uparrow v}$ is the up-sampling operation by v. It is assumed that the filter $w_v^p(t) = \beta^p\left(\frac{t}{v}\right)$ and the asterisk * denotes the convolution operator. After incorporating B-spline approximation, the solution of $q(j)$ is obtained as:

$$q(j) = \left\{c_v^p\right\}_{\downarrow v}(j) \tag{14}$$

where $\left\{c_v^p\right\}_{\downarrow v}$ is the down-sampling operation by v and c_v^p is the pre-filter represented by

$$c_v^p = \left\{\left(\left\{w_v^p * w_v^p\right\}_{\downarrow v}\right)^{-1}\right\}_{\uparrow v} * w_v^p \tag{15}$$

The signal y is first band-limited through a pre-filter w_v^p. Next, the band-limited signal is decimated by a factor of v. Finally, the approximation is reconstructed using a post-filter w_v^p. In this paper, TVF-EMD is used to decompose a single accelerometric signal into multiple IMFs.

Figure 14 shows the modal frequencies and the corresponding damping ratios of the model DMR02, which have been obtained from the data collected by sensor 1, setup A. Figures 14a, c and e are the FFTs of the IMFs of the first three modes of the structure identified from using TVF-EMD method. Figures 14b, d and f illustrate the corresponding damping estimation based on the decay curve of their autocorrelation functions. A similar analysis is repeated for all the models. The typical results of two other models (i.e., DMC02 and DMS03) are shown in Figs. 15 and 16, respectively. It was observed that the third mode of DMS02 did not have considerable energy; therefore, it has not been identified by TVF-EMD.

For setups A and B, the average of natural frequencies for the estimated modes and the corresponding damping across four measurement channels of all the models are presented in Table 5. The Coefficient of Variation (CV) is used to represent the variation of the obtained parameters. It can be observed that the damping estimates have significantly larger variation, while the modal frequencies have negligible variation, which is consistent with the literature [29].

Values listed in Table 5 comply with values summarised in Table 4 estimated using the Welch method. Results obtained with setup A, show the first frequency was estimated in the range from 11.3 Hz (DMS03) to 12.2 Hz (DMR02). It was observed that for models with a rectangular and circular plan shape, the first frequency is slightly larger for a more curved roof (DMR02 and DMC02) than for a flatter roof (DMR01 and DMC01), contrary to what was

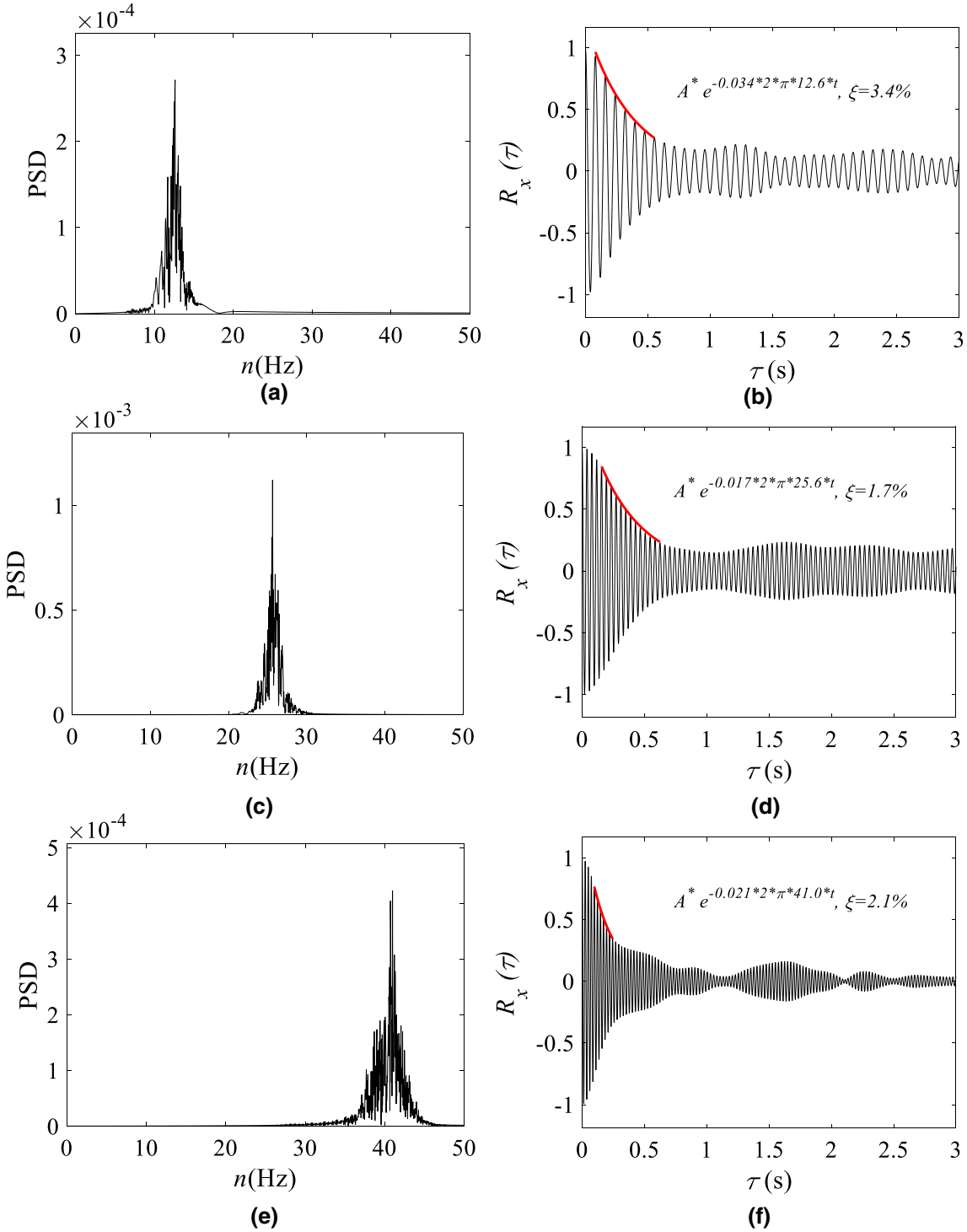

Fig. 14 Power spectral density (a^2/Hz) and ξ of the model DMR02 (Sensor-1) using TVF-EMD method; **a**, **b** FFT and autocorrelation function of IMF1; **c**, **d** FFT and autocorrelation function of IMF2; **e**, **f** FFT and autocorrelation function of IMF3, setup A

observed through the Welch method. Differently, the second estimated frequency is in the range of 24.5 Hz (DMS02) to 26.6 Hz (DMR01). The natural frequency of the third mode was estimated at around 41 Hz, but since it was impossible to estimate it for all the models it was neglected in this research.

The modal damping ratio for the first natural frequency ranges from 2.0% (DMR01) to 3.2 (DMS03), whereas for

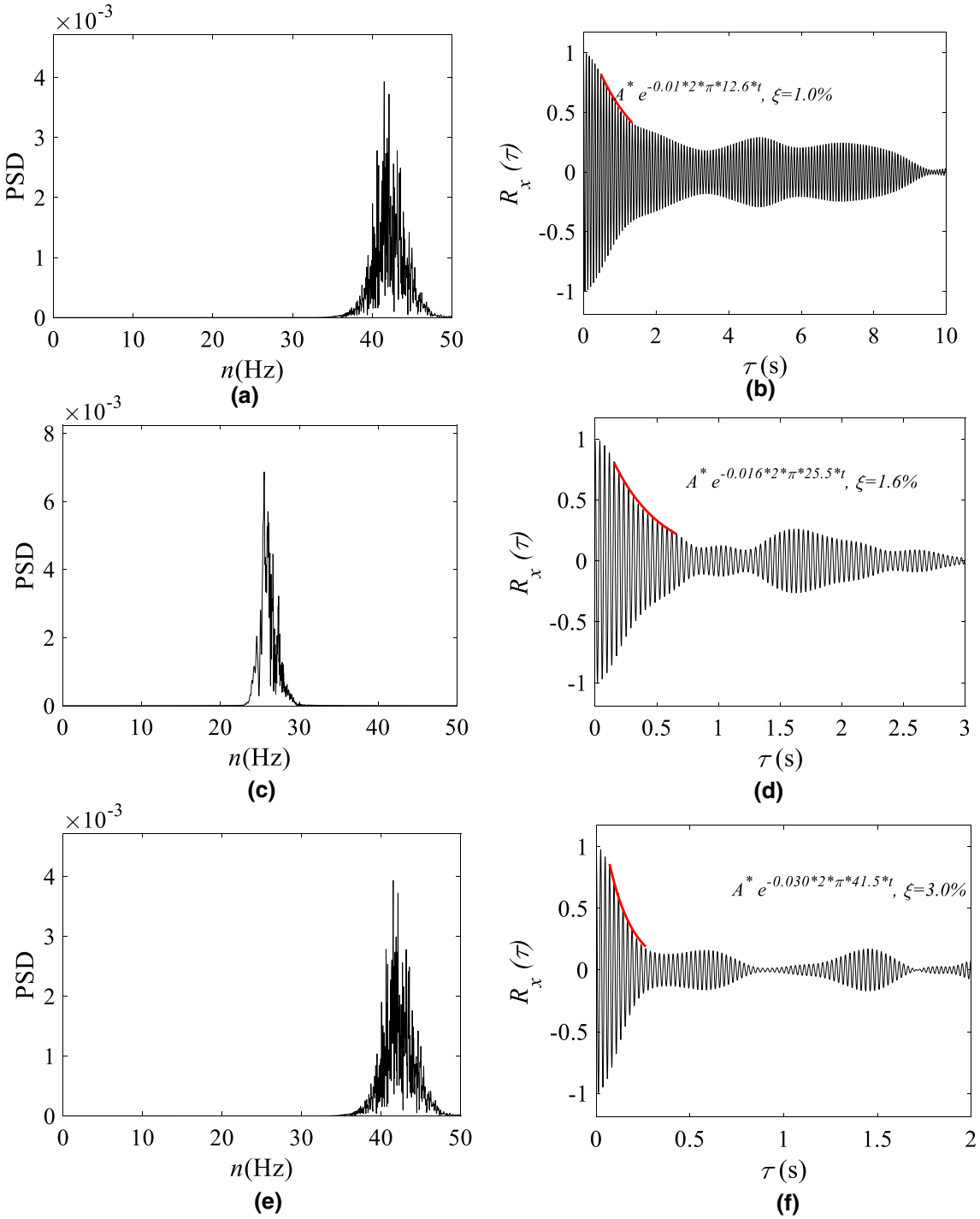

Fig. 15 Power spectral density (a^2/Hz) and ξ of the model DMC02 (Sensor-1) using TVF-EMD method; **a**, **b** FFT and autocorrelation function of IMF1; **c**, **d** FFT and autocorrelation function of IMF2; **e**, **f** FFT and autocorrelation function of IMF3, setup A

the second frequency, it ranges from 1.5% (DMR02) to 3.1% (DMC01). It was observed that model DMS03 has the largest damping ratio among the square plan models. This result is reasonable since the model has the heaviest mass on the roof. Regarding the damping ratio, the roof curvature does not seem to affect results significantly. Variations in damping ratios seem to be only related to random errors.

For sake of brevity, results obtained using setup B are only discussed for model DMS01. They give a frequency range between 6.56 and 19.44 Hz, very close to the first six frequencies estimated through Welch's method. A

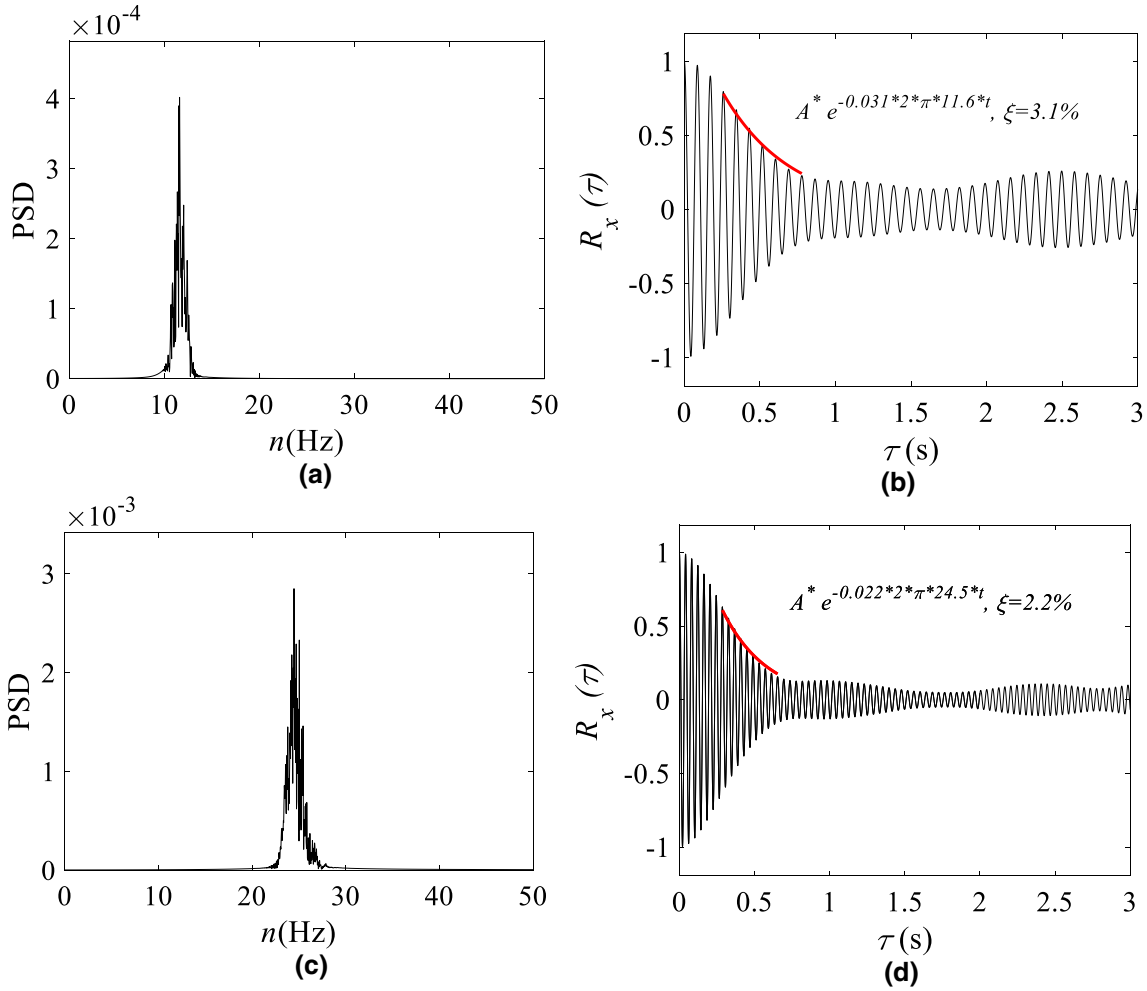

Fig. 16 Power spectral density (a^2/Hz) and ξ of the model DMS02 (Sensor-2) using TVF-EMD method; **a**, **b** FFT and autocorrelation function of IMF1; **c**, **d** FFT and autocorrelation function of IMF2, setup A

significantly high damping value was obtained for frequencies of 6.56 Hz and 9.52 Hz, namely 4.1% and 5.1%, respectively, whereas it was smaller for higher frequencies. The same trend was observed for measurements acquired through setup A.

4.4 Test model modes estimation via FDD

The frequency domain decomposition (FDD) approach was used to obtain a visualization of the most important test model modes. Figures 17, 18 and 19 show some examples of structural modes for a square plan (Fig. 17), a rectangular plan (Fig. 18) and a circular plan (Fig. 19) roof qualitatively compared with prototype modes. The cross-power spectral (CPSD) matrices were computed by selecting frequencies given by the RTD method (Table 4) and modal analyses were computed through the Singular Value Decomposition of the CPSD [31–34]. In Figs. 17, 18 and 19, circles highlight similar peaks in the deformed modal shape and the dotted line means the corresponding area investigated through sensors on the test model.

Figure 17 shows the modes #1 and #6 estimated through FDD (i.e. model) and FEM modal analyses (i.e. Prototype) for a square plan roof with geometry DMS01. It was observed that several peaks and valleys are in agreement between models and prototypes and it allowed for reliable calibration of predicted numerical scaled models. The same results were obtained for rectangular (Fig. 18) and circular (Fig. 19) plan roofs.

5 FEM predictive scaled models

To predict undesired and excessive roof deformation in a wind tunnel due to large wind velocity, a predictive FEM model was computed and calibrated at the experimental model scale. FEM modal analyses using TENSO [4] were performed to estimate the natural frequencies and the participating mass

Table 5 Estimation of modal frequencies (Hz) and damping (%) via TVF-EMD

	Mode	DMS01		DMS02		DMS03		DMR01		DMR02		DMC01		DMC02	
		n (Hz) (CV %)	ξ (%) (CV %)	*n* (Hz) (CV %)	ξ(%) (CV %)	*n* (Hz) (CV %)	ξ (%) (CV %)	*n* (Hz) (CV %)	ξ (%) (CV %)	*n* (Hz) (CV %)	ξ (%) (CV %)	*n* (Hz) (CV %)	ξ (%) (CV %)	*n* (Hz) (CV %)	ξ (%) (CV %)
Setup A	#1	12.0 (4.6)	2.2 (45.4)	11.6 (0.1)	3.1 (0.1)	11.3 (0.1)	3.2 (0.1)	11.9 (2.2)	2.0 (28.7)	12.2 (3.2)	2.7 (30.6)	11.6 (0.9)	2.8 (12.6)	12.1 (4.5)	2.5 (71.9)
	#2	25.7 (0.2)	1.7 (57.5)	24.5 (0.3)	1.8 (16.4)	25.6 (1.3)	2.9 (17.1)	26.6 (0.2)	1.6 (19.4)	26.1 (1.4)	1.5 (20.7)	25.2 (0.6)	3.1 (60.7)	25.6 (0.7)	1.9 (27.6)
	#3	41.1 (0.1)	2.6 (0.1)	– –	– –	41.8 (1.4)	3.1 (7.9)	– –	– –	41.0 (0.0)	2.2 (0.1)	– –	– –	41.5 (0.1)	3.8 (22.4)
Setup B	#1	6.56 (0.1)	4.1 (0.1)												
	#2	9.52 (0.1)	5.1 (0.1)												
	#3	11.08 (0.1)	1.1 (0.1)												
	#4	17.58 (0.1)	2.8 (0.1)												
	#5	19.44 (0.1)	2.0 (0.1)												

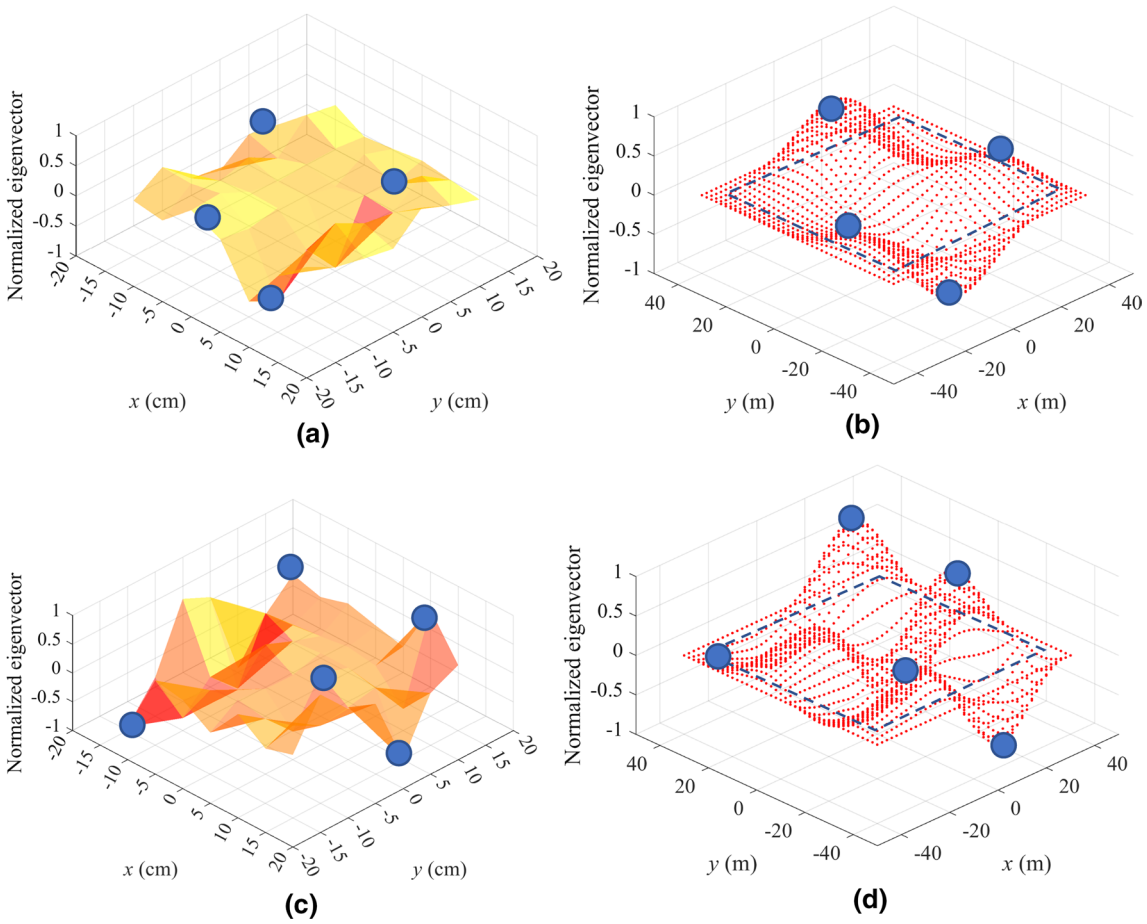

Fig. 17 DMS01 structural modes, mode #1 test model (**a**) and prototype (**b**), mode #6 test model (**c**) and prototype (**d**)

ratios, listed in Table 6, and to evaluate the deformed modal shapes, useful to design the sensors setup, for all geometries investigated in this research. The mean value of the smallest n_i and the largest n_u natural frequencies estimated by both FFT and EMD for all geometries and setups A were used to calibrate the predictive FEM model. The target values adopted to calibrate the predictive FEM models are summarised in Table 7.

After calibration, a decrease of 3% of the Young modulus of cables was introduced compared to the value reported in Sect. 3.2 ($1.64 \bullet 10^4$ MPa). The smallest and the largest natural frequencies computed by FEM (i.e. listed in Table 6) were named $n_{i,\mathrm{FEM}}$ and $n_{u,\mathrm{FEM}}$, respectively.

The relative error in percentage $RE_{\%}$ was estimated as Eq. (16) and assumed as a measure of the predicted model reliability

$$100 \bullet [(\eta(FEM) - \eta(EXP.)]/\eta(EXP.) \tag{16}$$

In Eq. (16), $\eta(FEM)$ is the first and the last natural frequency provided in Table 6, $\eta(EXP)$ is the first and the second natural frequency provided in Table 7. It was estimated that $RE_{\%}$ ranges from 0.1% to 4.18% (Fig. 20).

6 Wind tunnel aeroelastic tests design

The wind tunnel velocity scale λ_u was computed according to the aeroelastic criteria given by Eq. (4) for both the smallest n_i and the largest n_u natural frequencies at the model scale. Tables 8 and 9 summarise the scaling of models for both the smallest n_i (Table 8) and the largest n_u (Table 9), estimated through experiments and the smallest $n_{i,\mathrm{FEM}}$ (Table 10) and

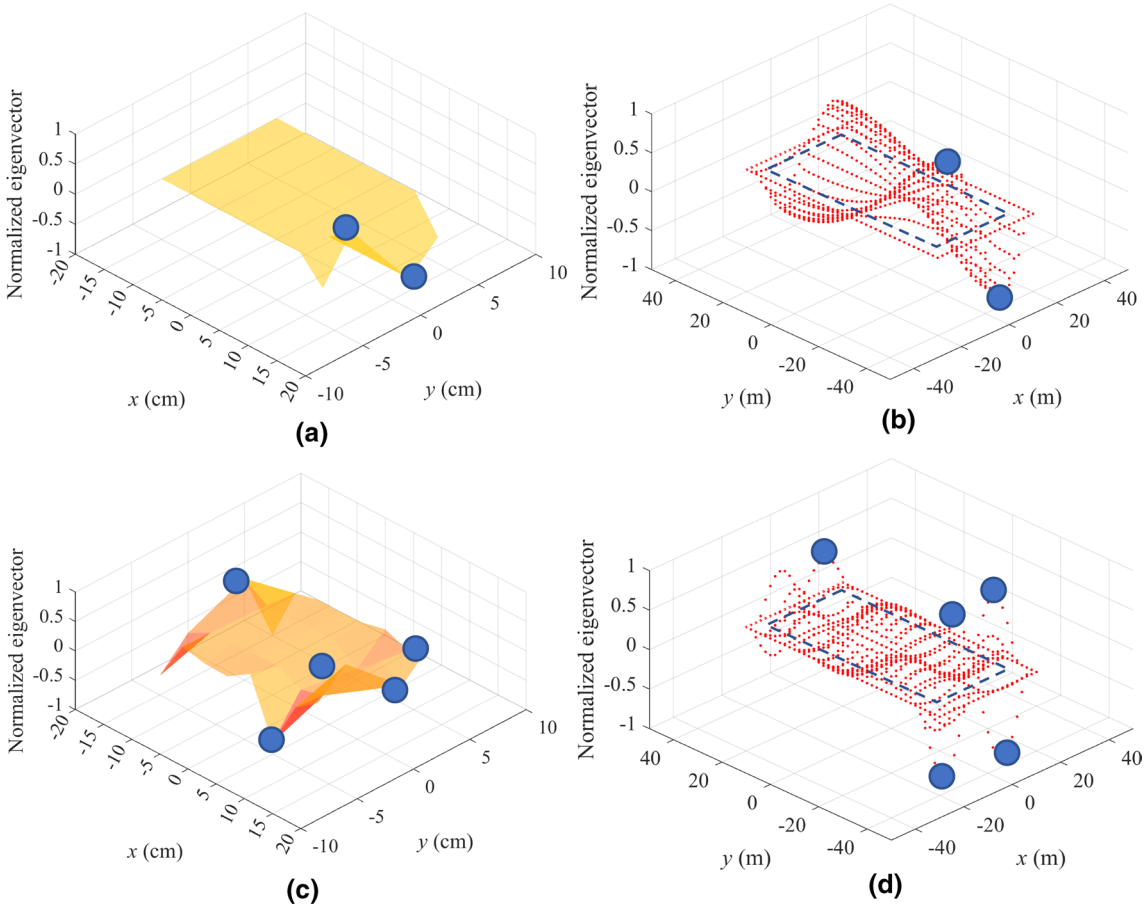

Fig. 18 DMR01 structural modes, mode #1 test model (**a**) and prototype (**b**), mode #10 test model (**c**) and prototype (**d**)

the largest $n_{u,\mathrm{FEM}}$ (Table 11) obtained by predictive FEM model at the model scale, where n is the natural frequency, l is the maximum plan side dimension, t is the time, U is the wind velocity at the roof height and finally, λ_t is the time scale, respectively.

The 10-min mean wind velocity at the prototype scale was calculated based on the EN1991-1–4 (2005), adopting the roughness length z_0 equal to 0.05 m, the directional factor c_{dir} and the season factor c_{season} equal to 1, the minimum height $z_{\min}$ equal to 2 m, turbulence factor k_I was equal to 1 and $z_{\max}$ was equal to 200 m. The wind velocity was calculated at the middle point of the roof that at the prototype scale was equal to 18.7 m (DMS01, DMR01, DMC01) and 22.2 m (DMS02, DMS03, DMR02, DMC02). The basic velocity defined as a function of the wind direction and the time of the year at 10 m above the ground of terrain category II was adopted as equal to 32 m/s, which is the maximum value given by EN1991-1-4 (2005) for Europe. According to EN1991-1-4 (2005), the mean velocity $v_m(z)$ was equal to 36 m/s for flat roofs (DMS01, DMR01, DMC01) and 37 m/s for more curved roofs (DMS02, DMS03, DMR02, DMC02).

Based on calculations, the mean velocity at the roof height in the wind tunnel should range between 9.16 and 24.66 m/s using natural frequencies n_i and $n_{i,\mathrm{FEM}}$ and between 19.49 m/s and 56.40 m/s using natural frequencies n_u and $n_{u,\mathrm{FEM}}$. The corresponding base velocity for each geometry is given in Table 12. The base velocity in the wind tunnel at the model scale should range between 8.14 and 21.29 m/s using natural frequencies n_i and $n_{i,\mathrm{FEM}}$ and between 17.32 and 48.69 m/s using natural frequencies n_u and $n_{u,\mathrm{FEM}}$.

6.1 Wind-induced displacements prediction

The expected wind-induced vertical displacements on both the test models and the prototype structures were estimated through geometrical nonlinear analyses using TENSO. The wind loads were computed from pressure coefficients provided by [21] and using the mean velocity given in Sect. 6.1 and they were applied as concentrated static forces to the cable net nodes. For the sake of brevity, only the results obtained using the scaling given in Table 8 for n_i are discussed in this section.

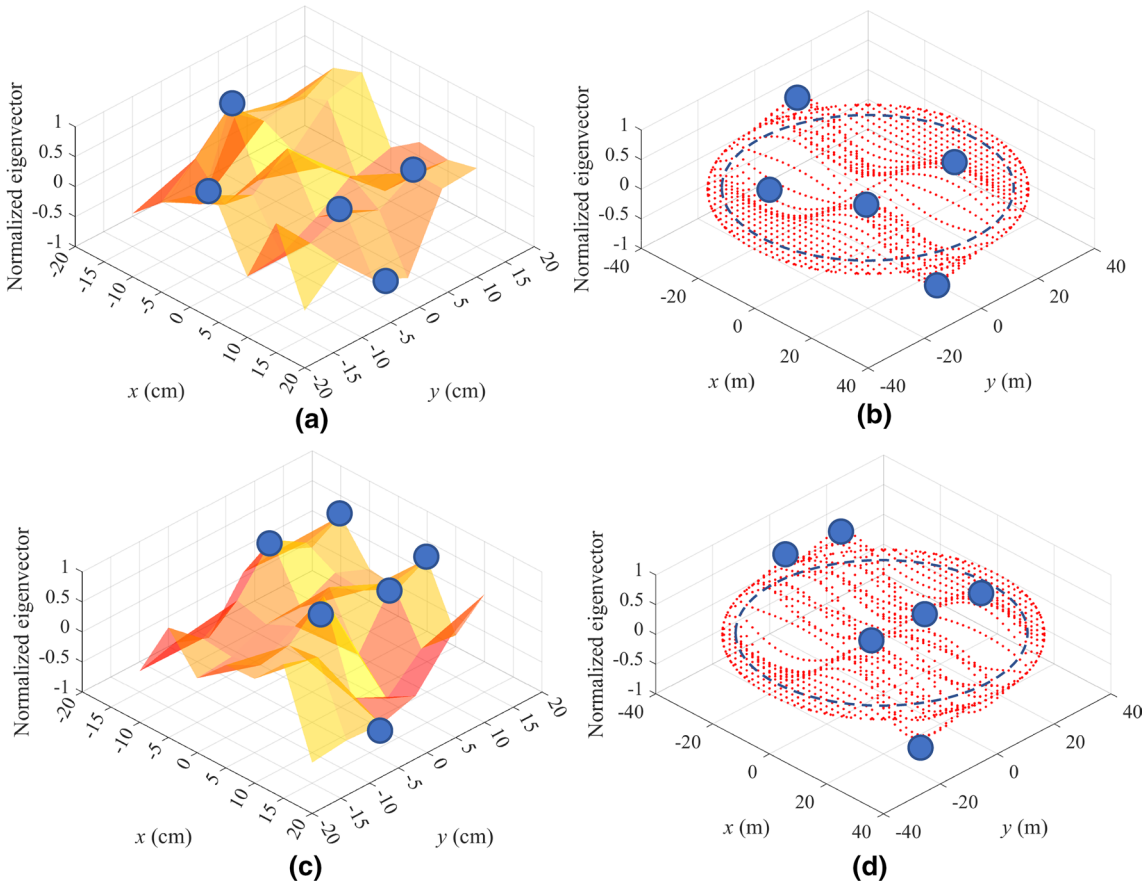

Fig. 19 DMC01 structural modes, mode #1 test model (**a**) and prototype (**b**), mode #4 test model (**c**) and prototype (**d**)

Table 6 Natural frequencies estimated through FEM modal analyses on the scaled predictive numerical model

Mode	DMS01		DMS02		DMS03		DMR01		DMR02		DMC01		DMC02	
	n (Hz)	Mp (%)	*n* (Hz)	Mp (%)	*n* (Hz)	Mp (%)	*n* (Hz)	Mp (%)	*n* (Hz)	Mp (%)	*n* (Hz)	Mp (%)	*n* (Hz)	Mp (%)
#1	11.9	0.7	11.2	2.9	11.5	1.0	11.9	11.8	12.0	0.6	11.8	0.0	11.9	0.0
#2	12.6	0.0	12.4	4.3	12.7	0.0	12.7	0.3	13.4	0.2	12.6	0.0	13.5	0.0
#3	13.7	0.5	14.1	3.0	14.5	0.2	13.9	0.3	15.6	5.1	13.7	0.0	15.3	0.0
#4	14.9	0.0	15.4	0.6	15.7	0.0	15.2	9.1	16.6	2.6	14.6	0.0	16.1	0.0
#5	16.4	0.0	15.8	8.1	16.3	1.6	16.7	1.4	17.6	7.7	15.7	0.0	16.9	0.0
#6	16.4	1.1	16.3	38.6	16.6	45.6	16.7	2.2	17.7	34.0	16.2	0.0	17.6	10.4
#7	17.0	33.5	17.7	0.0	18.1	0.6	17.2	43.8	19.4	6.6	16.6	0.0	18.8	0.0
#8	17.8	0.1	17.8	0.0	18.4	1.6	18.2	1.5	20.1	0.9	17.7	0.2	19.3	0.0
#9	18.7	0.0	19.0	15.9	19.5	25.1	18.2	1.5	21.1	15.8	19.6	36.5	20.5	0.0
#10	19.7	24.9	19.8	0.0	20.4	3.5	21.0	7.2	22.3	0.0	20.8	0.2	20.9	7.3
#11	20.3	1.2	20.9	0.0	21.3	0.2	22.0	1.8	22.4	0.1	21.5	0.0	21.6	0.2
#12	21.0	0.3	20.8	2.1	21.3	2.0	22.4	9.1	23.1	0.9	22.7	0.2	22.3	0.0
#13	21.9	1.5	21.6	0.3	22.0	0.0	23.8	0.1	23.1	0.8	21.8	59.3	22.6	0.0
#14	22.2	31.9	22.0	0.4	22.7	0.3	23.8	4.4	24.4	0.0	22.9	0.2	23.0	0.0
#15	23.8	0.1	22.6	7.6	23.1	1.9	24.9	0.1	25.0	0.8	23.9	0.1	24.1	1.5
#16	23.7	2.6	22.5	15.4	23.1	11.5	25.4	1.4	25.2	22.3	24.0	3.2	24.6	0.7
#17	23.7	0.6	23.8	0.0	24.3	0.9	25.6	1.6	25.7	0.3	25.1	0.1	24.2	79.4
#18	24.2	0.9	24.0	0.7	24.8	1.5	25.5	2.3	27.2	0.3	25.3	0.0	25.9	0.4
#19	24.9	0.1	24.4	0.3	25.1	2.3	26.2	0.2	27.4	1.1	25.2	0.0	26.1	0.0

Table 7 Target values of the smallest n_i and the biggest n_u natural frequency at the model scale estimated by experimental tests

	DMS01	DMS02	DMS03	DMR01	DMR02	DMC01	DMC02
n_i	11.8	11.2	11.4	11.9	12.0	11.7	11.8
n_u	25.8	24.7	25.1	26.7	26.3	26.0	26.0

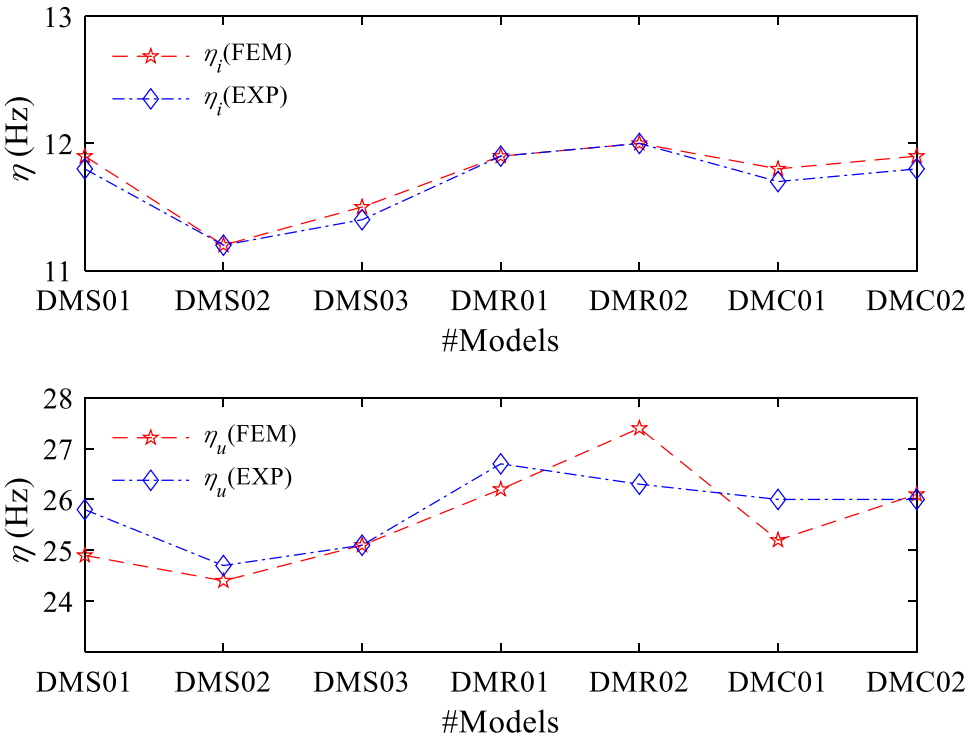

Fig. 20 Natural frequencies comparison between predicted FEM model and experimental test model

Table 8 Scaling parameters based on n_i

		DMS01	DMS02	DMS03	DMR01	DMR02	DMC01	DMC02
Prototype	n	0.23	0.18	0.18	0.12	0.09	0.23	0.18
Model		11.80	11.20	11.40	11.90	12.00	11.70	11.80
Scale	λ_n	51.30	62.22	63.33	99.17	133.33	50.87	65.56
Prototype	l	80.0	80.0	80.0	80.0	80.0	80.0	80.0
Model		0.40	0.40	0.40	0.40	0.40	0.40	0.40
Scale	λ_l	0.005	0.005	0.005	0.005	0.005	0.005	0.005
Prototype	t	2.2	2.2	2.2	2.2	2.2	2.2	2.2
Model		4.3E−02	3.5E−02	3.4E−02	2.2E−02	1.6E−02	4.4E−02	3.3E−02
Scale	λ_t	0.019	0.016	0.016	0.010	0.008	0.020	0.015
Prototype	m	125,523.90	128,022.98	128,022.98	62,761.95	64,011.49	97,908.65	99,857.93
Model		0.016	0.016	0.016	0.008	0.004	0.012	0.012
Scale	λ_m	1.25E−07	1.25E−07	1.25E−07	1.25E−07	1.25E−07	1.25E−07	1.25E−07
Prototype	U	36.00	37.00	37.00	36.00	37.00	36.00	37.00
Model		9.23	11.51	11.71	17.85	24.66	9.16	12.13
Scale	λ_u	0.257	0.311	0.317	0.496	0.667	0.254	0.328

Figures 21a and 22a show a three-dimensional view of the wind forces applied on the model DMS01 at the prototype and model scale, respectively, for the wind direction equal to 0° (Fig. 2), Figs. 21c and 22c show the wind loads distribution for the wind direction equal to 90°. Figures 21b, d, 22b and d present the corresponding wind-induced

Table 9 Scaling parameters based on n_u

		DMS01	DMS02	DMS03	DMR01	DMR02	DMC01	DMC02
Prototype	n	0.23	0.18	0.18	0.12	0.09	0.23	0.18
Model		25.80	24.70	25.10	26.70	26.30	26.00	26.00
Scale	λ_n	112.17	137.22	139.44	222.50	292.22	113.04	144.44
Prototype	l	80.00	80.00	80.00	80.00	80.00	80.00	80.00
Model		0.40	0.40	0.40	0.40	0.40	0.40	0.40
Scale	λ_l	0.005	0.005	0.005	0.005	0.005	0.005	0.005
Prototype	t	2.2	2.2	2.2	2.2	2.2	2.2	2.2
Model		2.0E−02	1.6E−02	1.6E−02	1.0E−02	7.4E−03	2.0E−02	1.5E−02
Scale	λ_t	0.009	0.007	0.007	0.004	0.003	0.009	0.007
Prototype	m	125,523.90	128,022.98	128,022.98	62,761.95	64,011.49	97,908.65	99,857.93
Model		0.016	0.016	0.016	0.008	0.004	0.012	0.012
Scale	λ_m	1.25E−07	1.25E−07	1.25E−07	1.25E−07	1.25E−07	1.25E−07	1.25E−07
Prototype	U	36.00	37.00	37.00	36.00	37.00	36.00	37.00
Model		20.19	25.38	25.79	40.05	54.06	20.35	26.71
Scale	λ_u	0.561	0.686	0.697	1.112	1.461	0.565	0.722

Table 10 Scaling parameters based on $n_{i,FEM}$

		DMS01	DMS02	DMS03	DMR01	DMR02	DMC01	DMC02
Prototype	n	0.23	0.18	0.18	0.12	0.09	0.23	0.18
Model		11.85	11.23	11.45	11.89	11.98	11.75	11.92
Scale	λ_n	51.52	62.39	63.61	99.08	133.11	51.09	66.22
Prototype	l	80.00	80.00	80.00	80.00	80.00	80.00	80.00
Model		0.40	0.40	0.40	0.40	0.40	0.40	0.40
Scale	λ_l	0.005	0.005	0.005	0.005	0.005	0.005	0.005
Prototype	t	2.2	2.2	2.2	2.2	2.2	2.2	2.2
Model		4.3E−02	3.5E−02	3.4E−02	2.2E−02	1.6E−02	4.4E−02	3.3E−02
Scale	λ_t	0.019	0.016	0.016	0.010	0.008	0.020	0.015
Prototype	m	125,523.90	128,022.98	128,022.98	62,761.95	64,011.49	97,908.65	99,857.93
Model		0.016	0.016	0.016	0.008	0.004	0.012	0.012
Scale	λ_m	1.25E−07	1.25E−07	1.25E−07	1.25E−07	1.25E−07	1.25E−07	1.25E−07
Prototype	U	36.00	37.00	37.00	36.00	37.00	36.00	37.00
Model		9.27	11.53	11.76	17.82	24.62	9.19	12.25
Scale	λ_u	0.258	0.312	0.318	0.495	0.665	0.255	0.331

vertical displacements at the prototype scale and model scale, respectively, for 0° and 90°.

The maximum and minimum values of the vertical displacements for all geometries are summarised in Table 13 and compared in Fig. 23 for the two wind angles, 0° and 90° (see Fig. 2 for details on the wind angles of attack). Positive values mean upward displacements, and negative values downward displacements. Results in Table 13 allowed us to validate the scale λ_l between the displacements estimated for the prototype and those estimated for the experimental model. If model DMS03 is excluded, the relative error in percentage, $RE_{\%}$, ranges between − 10.4 and 8.3%.

Table 11 Scaling parameters based on $n_{u,FEM}$

		DMS01	DMS02	DMS03	DMR01	DMR02	DMC01	DMC02
Prototype	n	0.23	0.18	0.18	0.12	0.09	0.23	0.18
Model		24.91	24.39	25.09	26.16	27.44	25.35	26.13
Scale	λ_n	108.29	135.50	139.39	217.98	304.89	110.20	145.17
Prototype	l	80.00	80.00	80.00	80.00	80.00	80.00	80.00
Model		0.40	0.40	0.40	0.40	0.40	0.40	0.40
Scale	λ_l	0.005	0.005	0.005	0.005	0.005	0.005	0.005
Prototype	t	2.2	2.2	2.2	2.2	2.2	2.2	2.2
Model		2.1E−02	1.6E−02	1.6E−02	1.0E−02	7.1E−03	2.0E−02	1.5E−02
Scale	λ_t	0.009	0.007	0.007	0.005	0.003	0.009	0.007
Prototype	m	125,523.90	128,022.98	128,022.98	62,761.95	64,011.49	97,908.65	99,857.93
Model		0.016	0.016	0.016	0.008	0.004	0.012	0.012
Scale	λ_m	1.25E−07	1.25E−07	1.25E−07	1.25E−07	1.25E−07	1.25E−07	1.25E−07
Prototype	U	36.00	37.00	37.00	36.00	37.00	36.00	37.00
Model		19.49	25.06	25.78	39.23	56.40	19.84	26.84
Scale	λ_u	0.541	0.677	0.697	1.090	1.524	0.551	0.725

Table 12 Base velocity in the wind tunnel at the model scale (values in m/s)

	DMS01	DMS02	DMS03	DMR01	DMR02	DMC01	DMC02
n_i	8.20	9.94	10.11	15.86	21.29	8.14	10.47
n_u	17.94	21.91	22.26	35.59	46.67	18.09	23.06
$n_{i,\mathrm{FEM}}$	8.24	9.95	10.15	15.84	21.25	8.17	10.58
$n_{u,\mathrm{FEM}}$	17.32	21.63	22.26	34.86	48.69	17.63	23.17

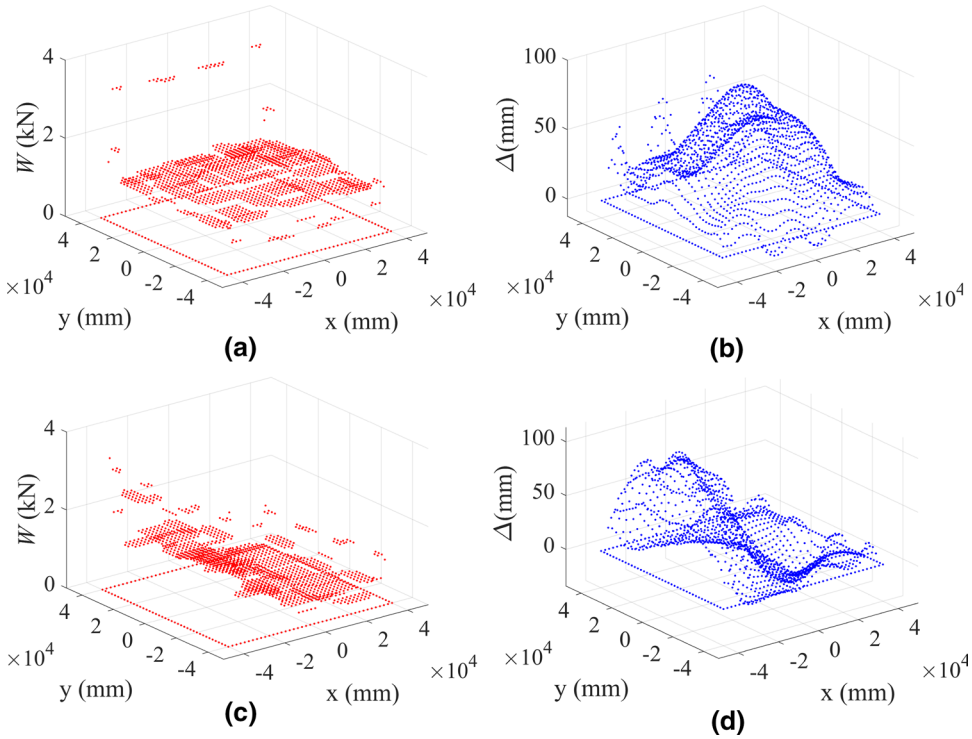

Fig. 21 Wind forces **a** and wind-induced vertical displacements **b** on the roof DMS01 with 0° and 90° **c** and **d** at the prototype scale, using the scaling provided in Table 8

It is worth noting that, even if the DMS03 mass scale is practically similar to one of the DMS02, the difference in terms of stiffness affects the results and the geometrical scale

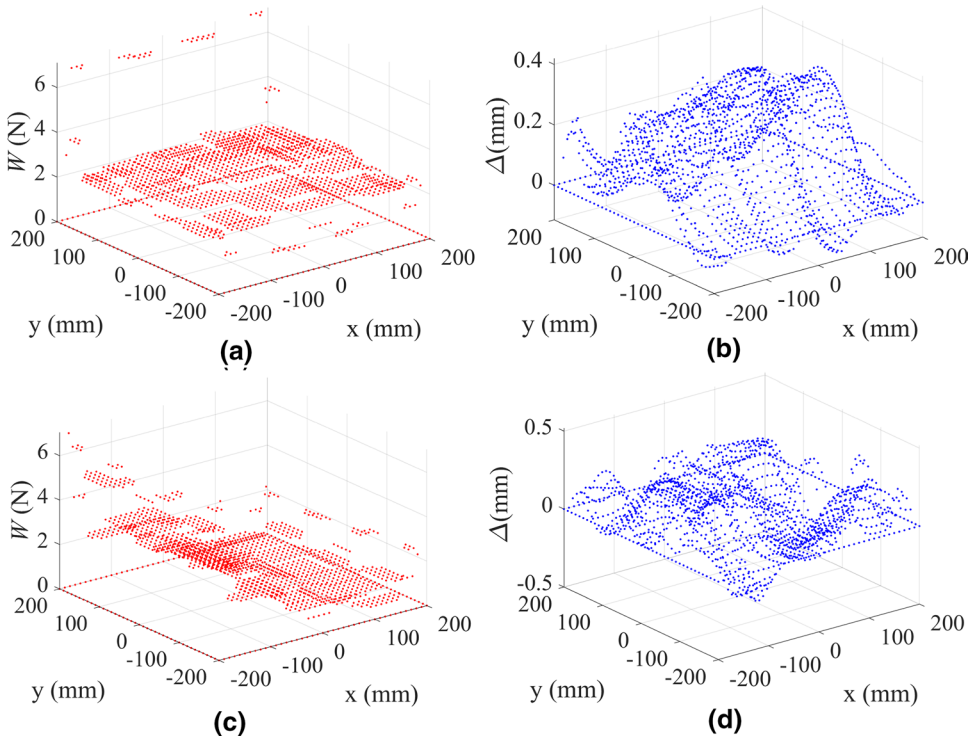

Fig. 22 Wind forces **a** and wind-induced vertical displacements **b** on the roof DMS01 with 0° and 90° **c** and **d** at the model scale, using the scaling provided in Table 8

Table 13 Maximum and minimum wind-induced vertical displacements on the experimental models (values in [mm]), using the scaling provided in Table 8

	Angle		DMS01	DMS02	DMS03	DMR01	DMR02	DMC01	DMC02
Prototype	0°	Max	87.82	132.9	132.9	31.89	65.86	80.79	122.27
		Min	− 22.43	− 9.32	− 9.32	− 44.10	− 58.52	− 20.41	− 8.48
	90°	Max	113.10	175.80	175.80	147.30	165.60	105.18	163.50
		Min	− 64.15	− 36.53	− 36.53	− 128.90	− 147.50	− 57.73	− 32.88
Model	0°	Max	0.43	0.65	0.58	0.16	0.32	0.39	0.60
		Min	− 0.11	− 0.05	− 0.04	− 0.22	− 0.29	− 0.10	− 0.04
	90°	Max	0.55	0.87	0.72	0.76	0.82	0.52	0.81
		Min	− 0.33	− 0.19	− 0.17	− 0.68	− 0.73	− 0.28	− 0.16

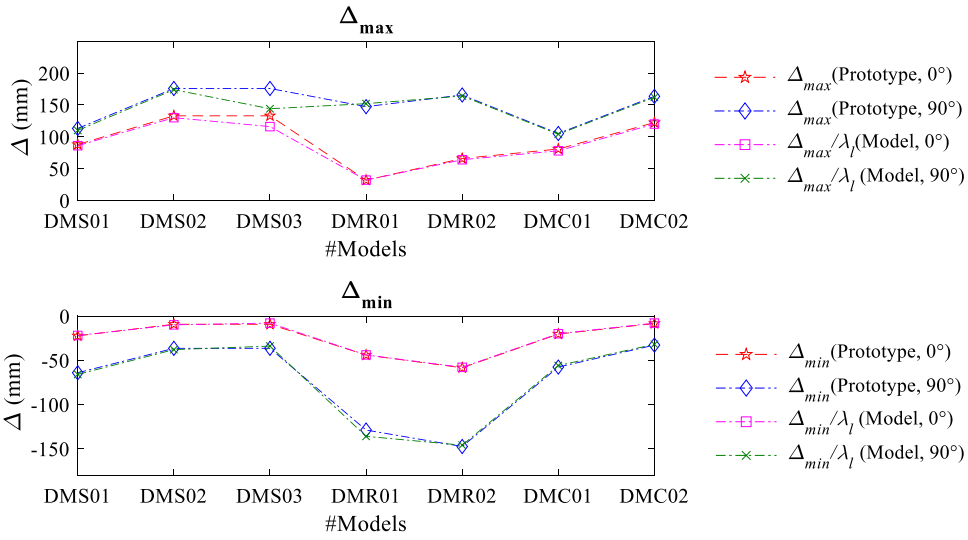

Fig. 23 Maximum and minimum wind-induced vertical displacements for 0° and 90° [mm]

is not valid in the case of DMS03, because the $RE_{\%}$ rages from 14.9 to 44.2%.

7 Conclusions

The aeroelastic test model construction of cable net and membrane roofs is a research challenge due to various technical difficulties, such as very small roof mass, small structural damping and a large number of natural frequencies which fall in a very narrow frequency range. As a consequence, very few wind tunnel studies were able to investigate wind-structure interaction phenomena characterizing the response of this special type of cable-supported roofs.

This paper contributes to filling this gap by proposing a test model construction method that allows precise modelling of each upward and downward cable assuming the correct internal traction to obtain the right geometrical shape. In addition, the cover that recreates the membrane is effectively linked to the net at the nodes. This approach allows the simulation of the correct cable net stiffness to obtain a good agreement in terms of natural frequencies and modal shapes between the experimental models and FEM analyses at a real scale.

Furthermore, careful dynamic identification of test models through different complementary mathematical approaches allowed us to observe that the higher modes involve the largest part of the roof, and this agrees with the modal analysis results on prototypes. Each test model was surrogated through a FEM model (at the model scale) to predict the wind–test model structure interaction in a wind tunnel. The predicted wind-induced displacements are very close to the wind-induced displacements estimated on the prototype with a relative error of about 10%.

Overall, the proposed construction method of aeroelastic models of cable net roofs is validated and represents an original way for accurately approximating the prototype cable net dynamic behaviour. However, the modelling of membrane-only roofs is still an open debate, and a further experimental campaign is necessary to validate the proposed approach for this roof typology.

Appendix 1: Signals processing via SVD

The Singular Value Decomposition (SVD) theorem states:

$$A_{nxp} = U_{nxn} \times S_{nxp} \times V_{pxp}^{T} \tag{17}$$

where the U_{nxn} columns are the left singular vectors (gene coefficient vectors); S_{nxp} (the same dimensions as A) has singular values and is diagonal (mode amplitudes); and V_{pxp}^{T} has rows that are the right singular vectors (expression level vectors) [30]. The SVD represents an expansion of the original data in a coordinate system where the covariance matrix is diagonal. Calculating the SVD consists of finding the eigenvalues and eigenvectors of $A_{nxp} \times A_{nxp}^{T}$ and $A_{nxp}^{T} \times A_{nxp}$. The eigenvectors of $A_{nxp}^{T} \times A_{nxp}$ make up the columns of V_{pxp}, the eigenvectors of $A_{nxp} \times A_{nxp}^{T}$ make up the columns of U_{nxp}. The singular values in S_{nxp} are also square roots of eigenvalues from $A_{nxp} \times A_{nxp}^{T}$ or $A_{nxp}^{T} \times A_{nxp}$. The singular values are the diagonal entries of the S_{nxp} matrix and are arranged in descending order. The singular values are always real numbers. If matrix A_{nxp} is a real matrix, then U_{nxn} and V_{pxp} are also real. The SVD was applied to signals acquired through setup B and, in this case A_{nxp} is a $480000 \times p$, where p is equal to 49 for square plan models, 44 for circular plan models and 40 for rectangular plan models.

The Normalised Diagonal of S_{nxp}, S is illustrated in Fig. 24 for all the geometries and significant differences were observed between models with different plan shape.

The different curvature affects the significance of the first eigenvector compared to the others. It was observed that for models with a more curved roof (i.e. DMS02, DR02 and DMC02) singular values of the first two eigenvectors represent 20% (Fig. 24b) of the total amount for the plan shape roofs, the 35% (Fig. 17d) for the rectangular plan shape and about 45% (Fig. 24f) for the circular plan shape roofs. For the rectangular plan roofs, the difference between more curved and flatter roofs is smaller than for the others.

Singular values decrease quickly from the third mode onwards for more curved roofs with a square and circular plan shape and for both, flatter and more curved roofs with a rectangular plan shape.

It can be stated that for more curved roofs only a few eigenvectors are the most significant whereas for flatter roofs, more flexible than the others, the differences between eigenvectors are too small. This result suggests that the dynamic identification of models with a flatter roof should be extended to as many modes as possible.

Figures 25, 26 and 27 show the eigenvectors plot for some significant modes for flatter roofs. Figure 24 illustrates the eigenvectors for modes #1, #6, #24 and #32 of model DMS01 and it was observed that the first mode involves only a small part of the entire roof.

A similar trend was observed for all plan shapes even if this effect decreases for rectangular plan roofs. Figure 26 shows the eigenvectors that involve only a part of the roof, moving along its surface.

Figure 27 illustrates the eigenvectors plot for the flatter roof with a circular plan shape and it was observed that the trend is similar to the square plan roofs. The eigenvectors that involve the largest part of the roof are the higher eigenvectors, for example, mode #18 illustrated in Fig. 27c.

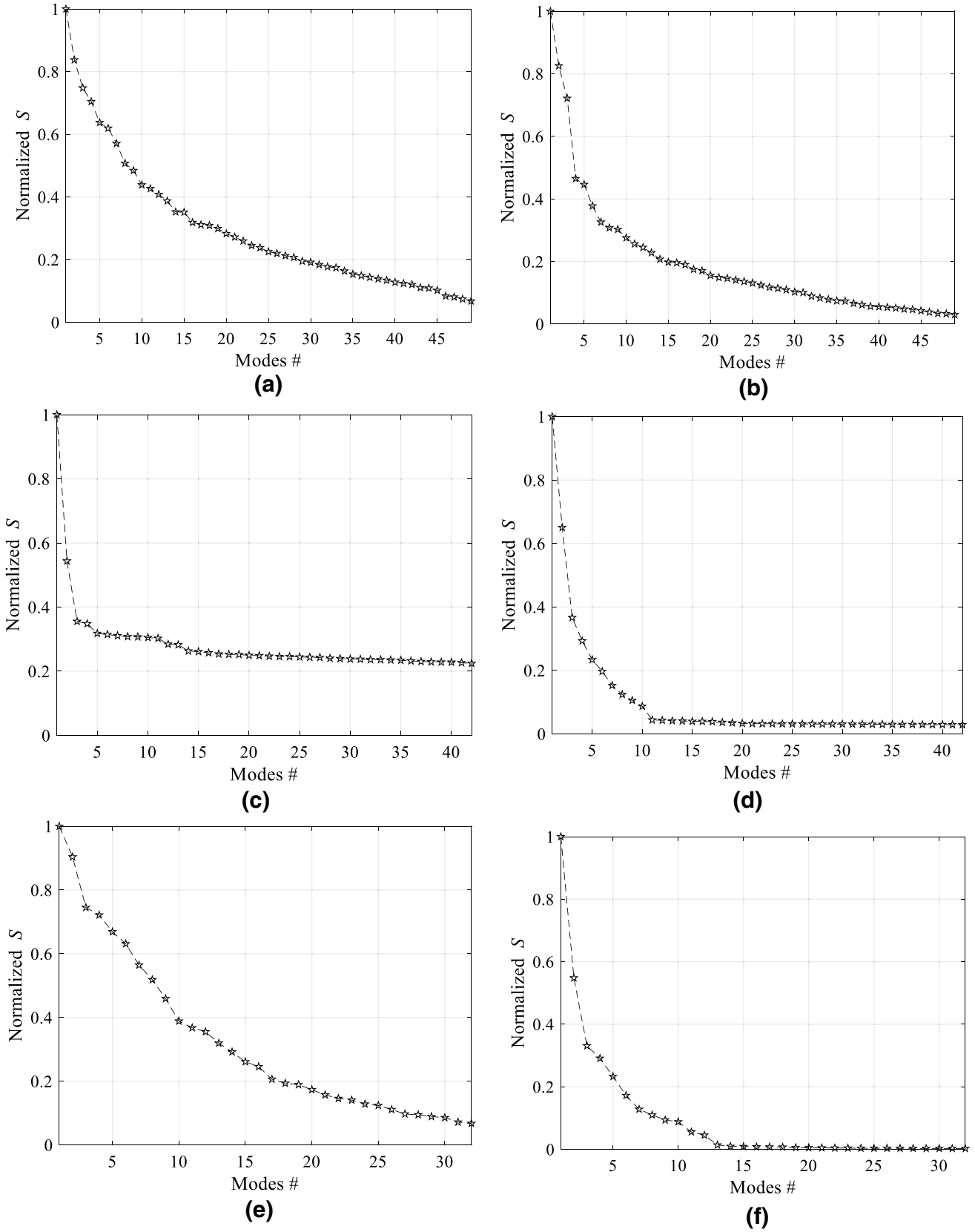

Fig. 24 Singular values of A for DMS01 (**a**), DMS02 (**b**), DR01 (**c**), DMR02 (**d**), DMC01 (**e**) and DMC02 (**f**)

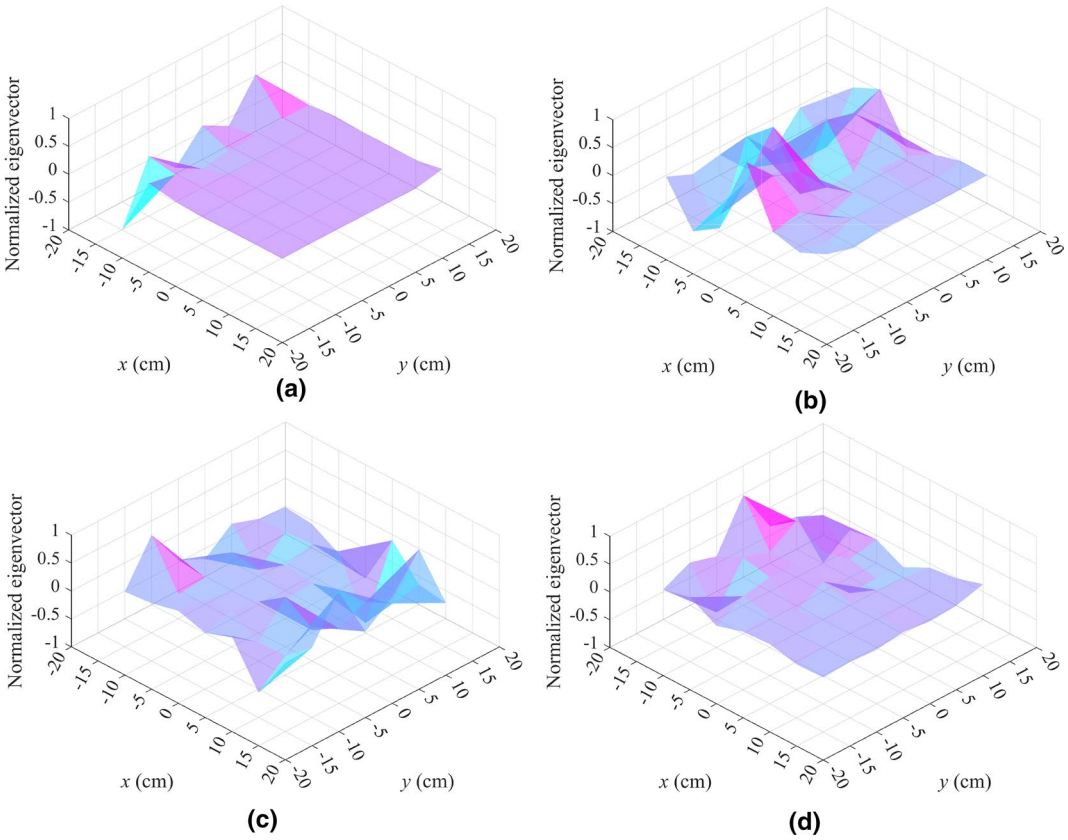

Fig. 25 Eigenvectors plot for DMS01 model, mode #1 (**a**), mode #6 (**b**), mode #24 (**c**) and mode #32 (**d**)

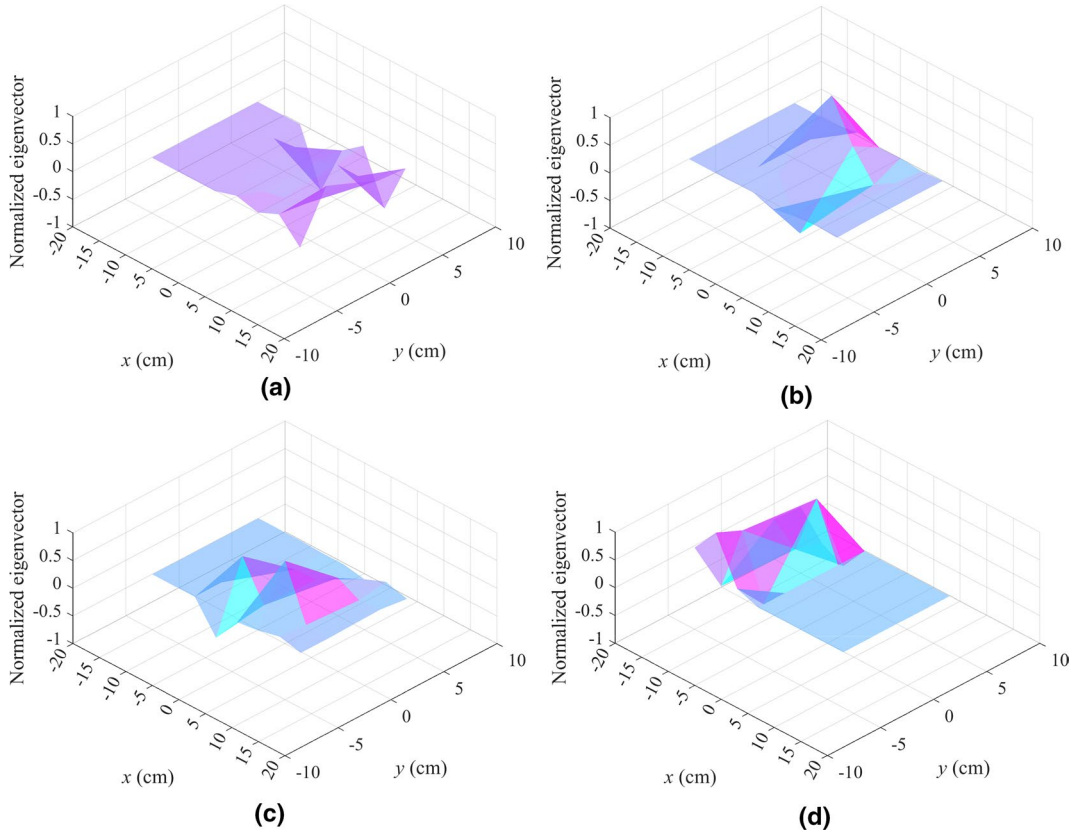

Fig. 26 Eigenvectors plot for DMR01 model, mode #1 (**a**), mode #5 (**b**), mode #24 (**c**) and mode #32 (**d**)

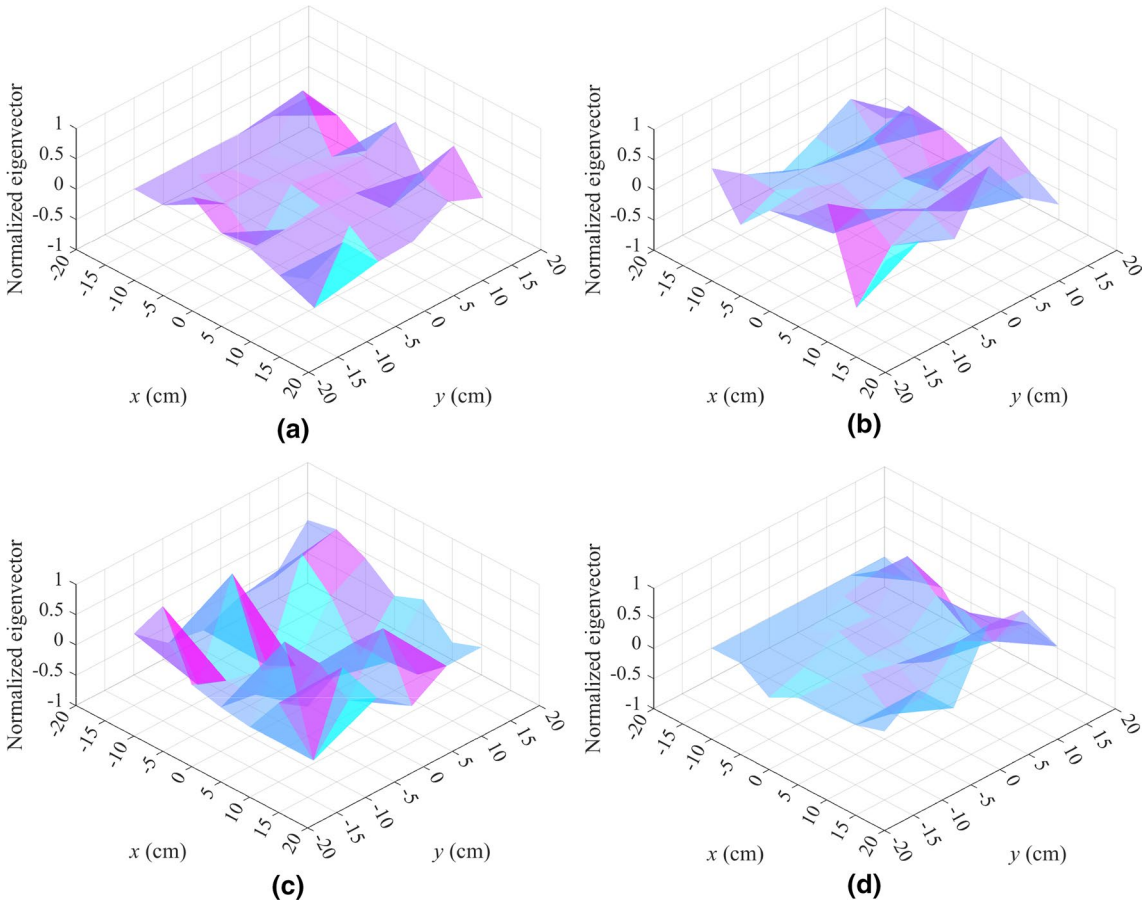

Fig. 27 Eigenvectors plot for DMC01 model mode #1 (**a**), mode #8 (**b**), mode #18 (**c**) and mode #32 (**d**)

Acknowledgements This research was supported by the Polish government through the Scholarship of the Polish National Agency for Academic Exchange (NAWA project, PPN/ULM/2020/1/00085). Model construction: PhD Maria Rita Guerrieri deserves to be thanked for her collaboration during experiments. The authors would like to thank the Multiassetlab.srl staff and Mr Davide Perazzetti for their support during the model construction.

Author contributions All authors have participated in: conception and design, or analysis and interpretation of the data; drafting the article or revising it critically for important intellectual content; approval of the final version.

Funding Open access funding provided by Politecnico di Bari within the CRUI-CARE Agreement. This study was funded by NAWA project, PPN/ULM/2020/1/00085.

Declarations

Conflict of interest Author Fabio Rizzo has received research grants from the Polish government through the Scholarship of the Polish National Agency for Academic Exchange.

Ethical approval This article does not contain any studies with human participants or animals performed by any of the authors.

References

1. Vassilopoulou I, Gantes CJ. Influence of a deformable contour ring on the nonlinear dynamic response of cable nets. Structures. 2016;6:146–58.
2. Vassilopoulou I, Petrini F, Gantes CJ. Nonlinear dynamic behavior of cable nets subjected to wind loading. Structures. 2017;10:170–83.
3. Rizzo F, Sepe V, Ricciardelli F, Avossa AM. Wind pressures on a large span canopy roof. Wind Struct. 2020;30(2):000–000.

4. Rizzo F, Caracoglia L. Examination of artificial neural networks to predict wind-induced displacements of cable net roofs. Eng Struct. 2021;245:112956.
5. Rizzo F, Sepe V. Static loads to simulate dynamic effects of wind on hyperbolic paraboloid roofs with square plan. J Wind Eng Ind Aerodyn. 2015;137:46–57.
6. CNR (National Research Council of Italy), 2018. CNR-DT207/2018. Guide for the Assessment of Wind Actions and Effects on Structures.
7. Rizzo F, D'Asdia P, Ricciardelli F, Bartoli G. Characterization of pressure coefficients on hyperbolic paraboloid roofs. J Wind Eng Ind Aerodyn. 2012;102:61–71.
8. Liu M, Chen X, Yang Q. Characteristics of dynamic pressures on a saddle type roof in various boundary layer flows. J Wind Eng Ind Aerodyn. 2016;150:1–14.
9. Colliers J, Mollaert M, Vierendeels J, De Laet L. Collating wind data for doubly-curved shapes of tensioned surface structures (round robin exercise 3). Procedia Eng. 2016;155:152–62.
10. Colliers J, Mollaert M, Degroote J, De Laet L. Prototyping of thin shell wind tunnel models to facilitate experimental wind load analysis on curved canopy structures. J Wind Eng Ind Aerodyn. 2019;188:308–22.
11. Colliers J, Degroote J, Mollaert M, De Laet L. Mean pressure coefficient distributions over hyperbolic paraboloid roof and canopy structures with different shape parameters in a uniform flow with very small turbulence. Eng Struct. 2020;205: 110043.
12. Rizzo F, Zazzini P, Montelpare S, Ricciutelli A. Investigation of wind induced vibration and acoustic performance interactions for a flexible roof through multiphysics approach. J Build Perform Simul. 2020;13(5):555–82.
13. Sun X, Wu Y, Yang Q, Shen S. Wind tunnel tests on the aeroelastic behaviors of tension structures. In: Proceedings of BBAA VI International Colloquium on: Bluff Bodies Aerodynamics & Applications, Milano, Italy, July, 20–24, 2008.
14. Sun X, Wu Y, Yang Q, Shen S. Wind tunnel tests on Levy Type cable dome. In: The Seventh Asia Pacific Conference on Wind Engineering, November 8–12, 2009, Taipei, Taiwan.
15. Yang Q, Wu Y, Zhu W. Experimental study on interaction between membrane structures and wind environment. Earthq Eng Eng Vib. 2010;9:4.
16. Rizzo F, Kopp AG, Giaccu G. Investigation of wind-induced dynamics of a cable net roof with aeroelastic wind tunnel tests. Eng Struct. 2021;229: 111569.
17. Elashkar I, Novak M. Wind tunnel studies of cable roofs. J Wind Eng Ind Aerodyn. 1983;13(1–3):407–19.
18. Uematsu Y, Uchiyama K. An elastic behaviour of an H.P. Shaped suspended roof. Shells, Membrane and Space Frames. In: Proceedings of IASS Symposium, Osaka, 2, pp 241–248.
19. Abbas RM, Abdulhameed AA, Salahaldin AI. Finite element analyses of hypar shell footing on elastic foundation. In: Proceedings of the 2nd International Conference on Geotechnical Engoineering (ICGE'10), Hammamet, Tunisia, October 25–27, October 2010.
20. Bairagi NK, Buragohain DN. Application of Finite element to hypar shell footings. In: Proceedings of the 2nd International Conference on Computer Aided Analyses and Design in Civil Engineering. III: 61–69 Roorkee.
21. Rizzo F, D'Asdia P, Lazzari M, Procino L. Wind action evaluation on tension roofs of hyperbolic paraboloid shape. Eng Struct. 2011;33(2):445–61 (**ISSN 0141-0296**).
22. CEN (Comité Européen de Normalization), 2005. EN1991-1-4: Eurocode 1: Actions on structures—Part 1–4: General actions—Wind actions.
23. Isyumov N. The aeroelastic modelling of tall buildings. In: Reinhold TA (ed) Proceedings of the international Workshop on Wind Tunnel Modelling Criteria and Technique in Civil Engineering Applications, Gaithersburg, Maryland, USA, April 1982. Cambridge University Press, Cambridge.
24. He XH, Huab XG, Chenb ZQ, Huang FL. EMD-based random decrement technique for modal parameter identification of an existing railway bridge. Eng Struct. 2011;33:1348–56.
25. Yang JN, Lei Y, Lin S, Huang N. Hilbert-Huang based approach for structural damage detection. J Eng Mech. 2004;130(1):85–95.
26. Yi TH, Li HN, Zhang XD. A modified monkey algorithm for optimal sensor placement in structural health monitoring. Smart Mater Struct. 2012;21(10): 105033.
27. Li Z, Park HS, Adeli H. New method for modal identification of super high-rise building structures using discretized synchro squeezed wavelet and Hilbert transforms: Super high-rise building structures. Struct Design Tall Spec Build. 2017;26(3):e1312.
28. Singh P, Keyvanlou M, Sadhu A. An improved time-varying empirical mode decomposition for structural condition assessment using limited sensors. Eng Struct. 2021;232: 111882.
29. Adhikari A. On the quantification of damping model uncertainty. J Sound Vib. 2007;306:153–71.
30. Tamura Y, Yoshida A, Zhang L, Ito T, Nakata S.Examples of modal identification of structures in Japan by FDD and MRD techniques. In: Naprstek J, Fischer C (eds) Proceedings of the EACWE4—The Fourth European and African Conference on Wind Engineering. ITAM AS CR, Prague, 11–15 July, 2005.
31. Brincker R, Zhang L, Andersen P. Modal identification from ambient responses using frequency domain decomposition. In: Proc. of the 18th International Modal Analysis Conference (IMAC), San Antonio, Texas, 2000.
32. Pastora M, Bindaa M, Harþarika T. Modal assurance criterion. Procedia Eng. 2012;48:543–8.
33. Fotsch D, Ewins DJ. Application of MAC in the frequency domain. Mechanical Engineering Department, Imperial College of Science, Technology and Medicine, London, UK.
34. Avilés R. The Modal Assurance Criterion (MAC). Bilbao 2009.